nature communications

Article

https://doi.org/10.1038/s41467-025-59685-3

Alternatively spliced mini-exon B in PTPδ regulates excitatory synapses through cell-type-specific trans-synaptic PTPδ-IL1RAP interaction

Received: 28 May 2024

Accepted: 30 April 2025

Published online: 13 May 2025

Check for updates

Seoyeong Kim[1,2,7], Jae Jin Shin[2,7], Muwon Kang[1,2,7], Yeji Yang[1,3], Yi Sul Cho[4], Hyojung Paik[5], Jimin Kim[5], Yunho Yi[1], Suho Lee[2], Hei Yeun Koo[6], Jinwoong Bok[6], Yong Chul Bae[4], Jin Young Kim[3] & Eunjoon Kim[1,2]

PTPδ, encoded by *PTPRD*, is implicated in various neurological, psychiatric, and neurodevelopmental disorders, but the underlying mechanisms remain unclear. PTPδ trans-synaptically interacts with multiple postsynaptic adhesion molecules, which involves its extracellular alternatively spliced mini-exons, meA and meB. While PTPδ-meA functions have been studied in vivo, PTPδ-meB has not been studied. Here, we report that, unlike homozygous PTPδ-meA-mutant mice, homozygous PTPδ-meB-mutant (*Ptprd-meB*$^{-/-}$) mice show markedly reduced early postnatal survival. Heterozygous *Ptprd-meB*$^{+/-}$ male mice show behavioral abnormalities and decreased excitatory synaptic density and transmission in dentate gyrus granule cells (DG-GCs). Proteomic analyses identify decreased postsynaptic density levels of IL1RAP, a known trans-synaptic partner of meB-containing PTPδ. Accordingly, IL1RAP-mutant mice show decreased excitatory synaptic transmission in DG-GCs. *Ptprd-meB*$^{+/-}$ DG interneurons with minimal IL1RAP expression show increased excitatory synaptic density and transmission. Therefore, PTPδ-meB is important for survival, synaptic, and behavioral phenotypes and regulates excitatory synapses in cell-type-specific and IL1RAP-dependent manners.

Synaptic adhesion molecules play critical roles in regulating synapse formation and function[1–8]. The LAR family of synaptic adhesion molecules known as LAR-receptor protein tyrosine phosphatases (LAR-RPTPs) contains three known members (PTPδ [encoded by *Ptprd*], PTPσ [*Ptprs*], and LAR [*Ptprf*])[9,10]. LAR-RPTPs are thought to be present mainly at presynaptic nerve terminals where they organize synaptic development and function through the tyrosine phosphatase activity and trans-synaptic interactions with postsynaptic adhesion molecules, including NGL-3, TrkC, Slitrks, IL1RAPL1, IL1RAP (also known as IL-1RAcP), SALM3/5 (LRFN4/5), and Neuroligin-3 (NLGN3)[9,11–22]. LAR-RPTPs are also thought to interact with pre-synaptic Neurexins and Netrin-G1 in a cis manner[23–25]. The structural

[1]Department of Biological Sciences, Korea Advanced Institute for Science and Technology (KAIST), Daejeon 34141, Korea. [2]Center for Synaptic Brain Dysfunctions, Institute for Basic Science (IBS), Daejeon 34141, Korea. [3]Digital Omics Research Center, Korea Basic Science Institute (KBSI), Ochang 28119, Korea. [4]Department of Anatomy and Neurobiology, School of Dentistry, Kyungpook National University, Daegu 41940, Korea. [5]Center for Biomedical Computing, Korea Institute of Science and Technology Information (KISTI), Daejeon 34141, Korea. [6]Department of Anatomy, Yonsei University College of Medicine, Seoul 03722, Korea. [7]These authors contributed equally: Seoyeong Kim, Jae Jin Shin, and Muwon Kang. e-mail: kime@kaist.ac.kr

bases of these trans-synaptic interactions were recently described in detail[26].

PTPδ differs from the other two LAR-RPTPs (PTPσ and LAR) in having been extensively associated with various brain disorders[27], including attention-deficit hyperactivity disorder (ADHD)[28–31], intellectual disability[32], restless leg syndrome[33–36], insomnia[37], addiction[38,39], bipolar disorder[40], obsessive-compulsive disorder[41,42], and anxiety[43]. Previous studies on homozygous PTPδ-mutant mice reported various disease-related behavioral phenotypes and synaptic changes[39,44,45]. Some recent reports have disagreed on whether LAR-RPTPs regulate synapse development, synaptic transmission, and synaptic receptor functions[46–49], although this may reflect differences in the studied spatiotemporal context.

A notable feature of LAR-RPTPs is that they contain short-peptide mini-exons at several locations of the protein, including mini-exons A and B (meA and meB, respectively) in the extracellular region[50]. meA and meB have been shown to regulate meA/meB-dependent trans-synaptic interactions with multiple postsynaptic binding partners[51–57]. For instance, PTPδ-meA regulates the interaction with IL1RAPL1[17,58], a postsynaptic adhesion molecule that regulates synaptic and neuronal functions[59], while PTPδ-meB regulates the interactions with Slitrks, SALM3/5 (Lrfn4/5), IL1RAP, and Neuroligin-3[11,12,15,16,18,19,52,54,58]. In vivo functions of PTPδ have been studied using mice that lack the whole PTPδ protein[39,44,45,49,60–63], but relatively little is known about the in vivo functions of PTPδ-meA and PTPδ-meB. Previous studies provided evidence that PTPδ-meA regulates excitatory synapses in a cell type, circuit, and activity-dependent manner and specific behaviors and cognitive functions (i.e., sleep and object-location memory)[45,49], but it remains unknown whether PTPδ-meB affects synaptic and/or brain functions in mice and how PTPδ-meB phenotypes compare with PTPδ-meA phenotypes. This status contrasts with the extensive body of knowledge around alternative splicing in neurexins and neuroligins[64–80].

In the present study, we generated mice that lack PTPδ-meB and compared their behavioral, synaptic, circuit, and molecular phenotypes with those of PTPδ-meA-mutant mice. Surprisingly, homozygous PTPδ-meB-mutant (*Ptprd-meB*$^{-/-}$) mice show substantially decreased early postnatal survival (~30% of normal levels); this phenotype is two-fold stronger than that of homozygous global PTPδ-mutant mice, and contrasts with the normal survival of homozygous PTPδ-meA-mutant (*Ptprd-meA*$^{-/-}$) mice. Heterozygous PTPδ-meB-mutant (*Ptprd-meB*$^{+/-}$) mice also show strongly reduced excitatory synaptic density and transmission in dentate gyrus granule cells (DG-GCs), whereas such synaptic phenotypes are not observed in heterozygous PTPδ-meA-mutant (*Ptprd-meA*$^{+/-}$) mice. Mechanistically, *Ptprd-meB*$^{+/-}$ mice display postsynaptic loss of IL1RAP (a trans-synaptic PTPδ partner) and, accordingly, IL1RAP deletion in mice causes excitatory synaptic deficits in DG-GCs similar to those seen in *Ptprd-meB*$^{+/-}$ mice. In contrast, excitatory synaptic transmission at DG interneurons (DG-INs) is increased in *Ptprd-meB*$^{+/-}$ mice, and the changes in DG-INs and DG-GCs together strongly suppress the ratio of excitatory/inhibitory synaptic inputs onto DG-GCs. This suggests that PTPδ-meB deletion in axon terminals can induce distinct excitatory synaptic effects on two different postsynaptic neurons (DG-GCs and DG-INs).

Results

Strong developmental and behavioral phenotypes are seen in *Ptprd-meB*$^{+/-}$ but not *Ptprd-meA*$^{+/-}$ mice

PTPδ's meA consists of 9 amino acids (3 amino acids in meA3 and 6 amino acids in meA6), and meB consists of 4 amino acids (Fig. 1a). Despite its short length, the meA and meB splice inserts in PTPδ are known to regulate its trans-synaptic interactions with postsynaptic adhesion molecules (Fig. 1b). To explore the in vivo functions of meB, we generated PTPδ-meB-mutant mice by deleting exon 18 of the *Ptprd* gene (Fig. 1c). This deletion did not affect the mRNA levels of neighboring non-target exons (exon 13 and meA-encoding exons 15 and 16) (Fig. 1d) or the total levels of the PTPδ protein (Fig. 1e). While heterozygous PTPδ-meB-mutant (*Ptprd-meB*$^{+/-}$) mice showed normal survival at P7, homozygous PTPδ-meB-mutant (*Ptprd-meB*$^{-/-}$) mice showed markedly decreased (~35% of the expected levels) survival at P7 but normal survival at E18 (Supplementary Fig. 1a,b), suggesting that *Ptprd-meB*$^{-/-}$ mice experience a substantial decrease in survival during early postnatal stages. In the previously reported PTPδ-meA-mutant and global PTPδ-mutant mice[45], homozygotes showed normal and moderately decreased (~70% of the expected levels) lethality, respectively, compared to controls (Supplementary Fig. 1c,d). These results suggest that the PTPδ-meB splice insert has substantial impacts on early postnatal survival in mice, whereas meA has few such impacts.

We next characterized the behavioral phenotypes of *Ptprd-meB*$^{+/-}$ mice and compared them with those of *Ptprd-meA*$^{+/-}$ mice. *Ptprd-meB*$^{+/-}$ mice showed decreased locomotor activity in the open-field test and increased anxiety-like behaviors in the open-field, light-dark, and elevated plus-maze tests (Fig. 1f–i). In contrast, *Ptprd-meA*$^{+/-}$ mice showed normal locomotion and anxiety-like behaviors (Fig. 1j–m), which differed from the reported hyperactivity and anxiolytic-like behaviors in the homozygous PTPδ-meA-mutant (*Ptprd-meA*$^{-/-}$) mice[45]. In the LABORAS test, which involves long-term measurement of mouse movements in a familiar environment, *Ptprd-meB*$^{+/-}$ but not *Ptprd-meA*$^{+/-}$ mice showed increased repetitive rearing but normal locomotor activities (Supplementary Fig. 2a–d). *Ptprd-meB*$^{+/-}$ but not *Ptprd-meA*$^{+/-}$ mice also showed a decreased acoustic startle response without alteration of baseline auditory function (Supplementary Fig. 2e–i). Female *Ptprd-meB*$^{+/-}$ mice showed behaviors largely similar to those observed in males, except that anxiety-like behavior was relatively weaker in females compared to males (Supplementary Fig. 3), where anxiety-modulatory sex-specific factors (i.e., chromosome/hormone) might be involved[81–84].

These results indicate that homozygous deletion of meB from the *Ptprd* gene leads to substantial suppression of mouse development and survival during early postnatal stages, and in the heterozygous state is associated with various behavioral abnormalities including hypoactivity, anxiety-like behavior, repetitive rearing, and reduced acoustic startle in mice. This contrasts with PTPδ-meA deletion, which has minimal impacts on developmental and behavioral phenotypes.

Opposite excitatory synaptic changes in *Ptprd-meB*$^{+/-}$ dentate granule cells and interneurons

PTPδ-tdTomato signals are seen in various brain regions, with particularly strong signals in entorhinal cortical (EC) nerve terminals of the hippocampal dentate gyrus; we previously reported these findings in juvenile PTPδ-tdTomato reporter mice[45] and herein confirmed them in adult PTPδ-tdTomato mice (Supplementary Fig. 4a,b). Since both DG-GCs and DG-INs can receive excitatory synaptic inputs from the EC, we sought to measure spontaneous and evoked synaptic transmissions these cells. Also, since the ventral hippocampus has been associated with anxiety-like behavior[85,86] and the EC-DG perforant pathway is better preserved in ventral hippocampal slices[87,88], we characterized neurons in the ventral (not dorsal) part of the DG (Supplementary Fig. 4c).

In experiments measuring spontaneous excitatory synaptic transmission in *Ptprd-meB*$^{+/-}$ mice, DG-GCs showed a significant decrease in the frequency of miniature excitatory postsynaptic currents (mEPSCs) without any change in their amplitude (Fig. 2a, b). This difference was not observed when spontaneous excitatory postsynaptic currents (sEPSCs) were measured in DG-GCs in the absence of

https://doi.org/10.1038/s41467-025-59685-3

tetrodotoxin (Fig. 2c), suggesting that network activity normalizes the difference in mEPSCs; Our data below indicate that this normalization may be due to increased presynaptic release from EC inputs. In contrast, miniature inhibitory postsynaptic currents (mIPSCs) were normal in DG-GCs (Fig. 2d). These findings indicate the existence of meB-specific excitatory synaptic changes. We also observed that *Ptprd-meA*$^{+/-}$ mice showed normal mEPSCs (Fig. 2e), suggesting that meB is more important than meA in this regard.

When DG-INs were measured for excitatory synaptic transmission (Supplementary Fig. 5a), we found that, in contrast to the decreased

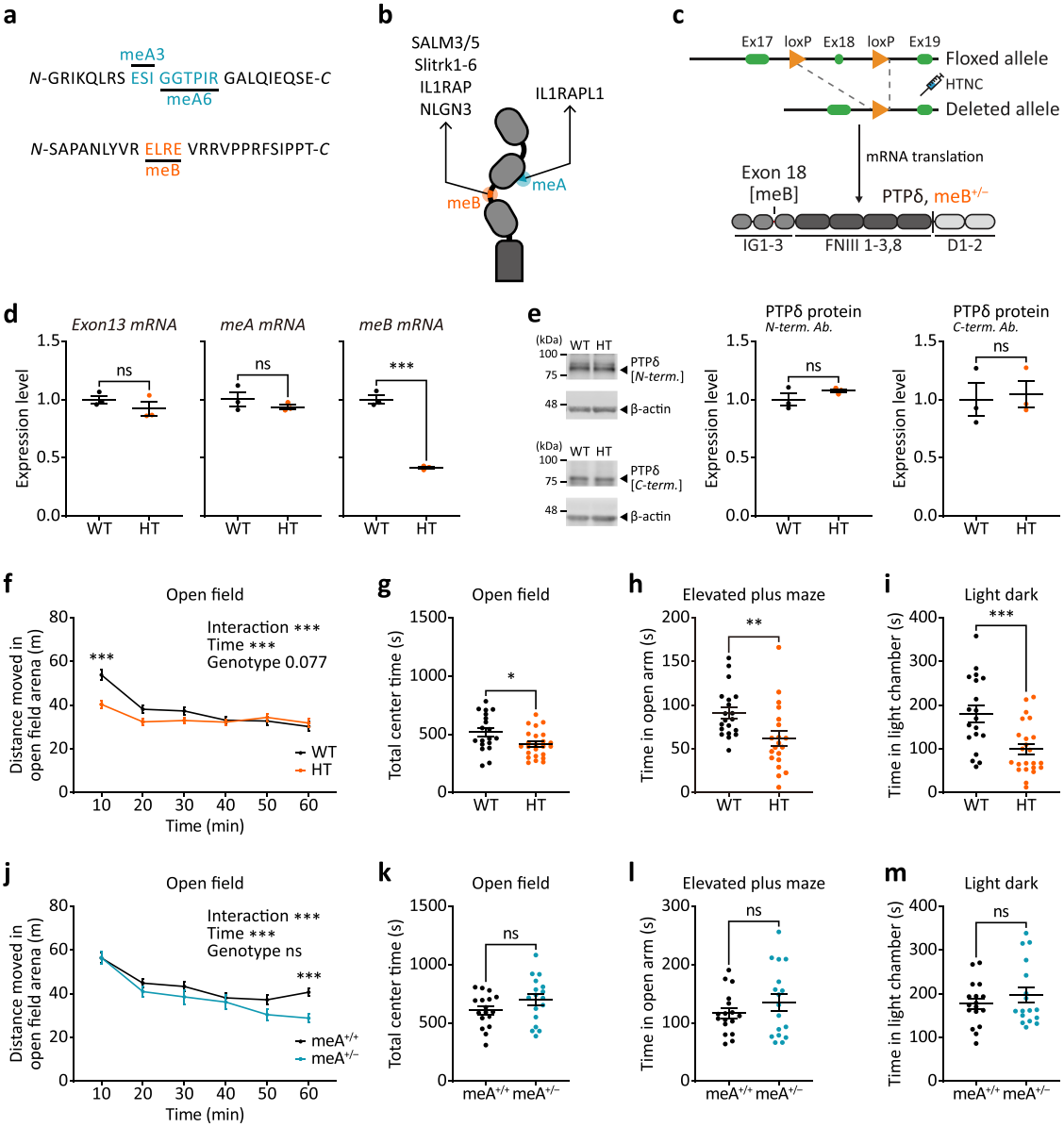

Fig. 1 | Distinct behavioral phenotypes of *Ptprd-meB*$^{+/-}$ and *Ptprd-meA*$^{+/-}$ mice. **a** The amino acid sequences of mini-exon A (meA) and mini-exon B (meB). The meA consists of two segments: meA3 and meA6, with three and six amino acids, respectively. **b** Schematic of meA and meB, which are located in the extracellular domain of PTPδ. They are required for the indicated meA/meB-dependent trans-synaptic interactions with postsynaptic molecules. An exception is NLGN3, which prefers meB-negative PTPδ. **c** Knockout strategy for meB (exon18) in PTPδ-meB-mutant (*Ptprd-meB*$^{+/-}$) mice. **d** Validation of meB knockout in *Ptprd-meB*$^{+/-}$ mice by RT-qPCR. Note that non-target exons (exon13 and meA) were not affected while meB levels were decreased by ~50% in *Ptprd-meB*$^{+/-}$ mice (P63; male; whole brain). ($n = 3$ mice [*Ptprd-meB*$^{+/+}$ (WT/wild-type), *Ptprd-meB*$^{+/-}$ (HT/heterozygous)], two-tailed Student's t-test, meB mRNA $P < 0.001$). **e** Normal PTPδ protein levels in *Ptprd-meB*$^{+/-}$ mice (P63; male; whole brain). PTPδ protein was detected using N-terminal (home-made, #2063) and C-terminal (home-made, #2061) antibodies. ($n = 3$ [WT, HT], two-tailed Student's *t*-test). **f** Hypoactivity of *Ptprd-meB*$^{+/-}$ mice (P56–84; male) in the open-field test (first 10 min). ($n = 19$ [WT], 24 [HT], two-way ANOVA with Holm-Sidak's test, Interaction $P < 0.001$, Time $P < 0.001$, 10 min $P < 0.001$). **g** Anxiety-like behavior of *Ptprd-meB*$^{+/-}$ mice (P56–84; male) measured by center time in the open-field test. ($n = 19$ [WT], 24 [HT], two-tailed Student's *t*-test, $P = 0.0182$). **h** Anxiety-like behavior of *Ptprd-meB*$^{+/-}$ mice (P56–84; male) measured by open-arm time in the elevated plus-maze test. ($n = 20$ [WT, HT], two-tailed Mann-Whitney test, $P = 0.0022$). **i** Anxiety-like behavior of *Ptprd-meB*$^{+/-}$ mice (P56–84; male) measured by light-chamber time in the light-dark test. ($n = 19$ [WT], 23 [HT], two-tailed Student's *t*-test, $P < 0.001$). **j** Normal open-field locomotion in *Ptprd-meA*$^{+/-}$ mice (P56–84; male). ($n = 17$ [meA$^{+/+}$, meA$^{+/-}$], two-way ANOVA with Holm-Sidak's test, Interaction $P < 0.001$, Time $P < 0.001$, 60 min $P < 0.001$). **k**–**m** Normal anxiety-like behavior of *Ptprd-meA*$^{+/-}$ mice (P56–84; male) in open-field, elevated plus-maze, and light-dark tests. ($n = 17$ [meA$^{+/+}$, meA$^{+/-}$], two-tailed Student's *t*-test [open-field and elevated plus-maze], two-tailed Mann–Whitney test [light-dark]). Data values represent means ± SEM. Significance is indicated as *(<0.05), **(<0.01), ***(<0.001), or ns (not significant). Source data are provided as a Source Data file.

https://doi.org/10.1038/s41467-025-59685-3

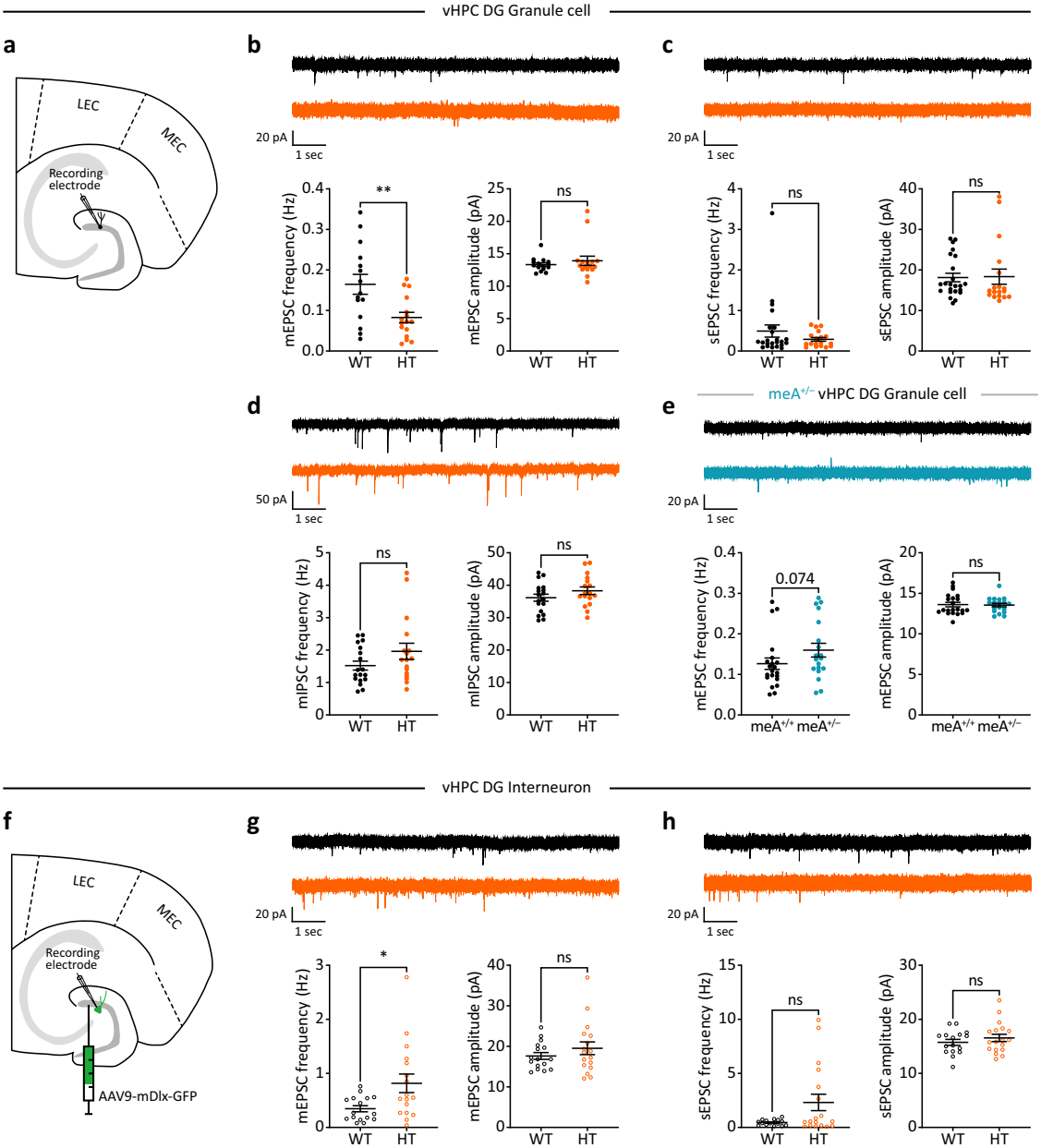

Fig. 2 | Opposite changes are seen in excitatory synaptic transmissions of *Ptprd-meB*$^{+/-}$ dentate granule cells versus interneurons. a Experimental scheme for measuring mE/IPSCs and sEPSCs in dentate gyrus granule cells (DG-GCs) from the ventral hippocampus (vHPC) of *Ptprd-meB*$^{+/-}$ mice (P56–70; male). M/LEC, medial/lateral entorhinal cortex. **b** mEPSC frequencies and amplitudes in WT and *Ptprd-meB*$^{+/-}$ DG-GCs (P56–70; male). (n = 15 neurons from 5 mice [WT],16, 5 [*Ptprd-meB*$^{+/-}$/HT], two-tailed Welch's t-test [frequency], two-tailed Mann–Whitney test [amplitude], Frequency P = 0.0075). **c** sEPSC frequencies and amplitudes in WT and *Ptprd-meB*$^{+/-}$ DG-GCs (P56–70; male). (n = 23, 6 [WT], 18, 7 [HT], two-tailed Mann-Whitney test). **d** mIPSC frequencies and amplitudes in WT and *Ptprd-meB*$^{+/-}$ DG-GCs (P56–70; male). (n = 18, 5 [WT], 17, 4 [HT], two-tailed Mann-Whitney test [frequency], two-tailed Student's t-test [amplitude]). **e** mEPSC frequencies and amplitudes in WT and *Ptprd-meA*$^{+/-}$ DG-GCs (P56–70; male). (n = 21, 4 [meA$^{+/+}$], 19, 3 [meA$^{+/-}$], two-tailed Mann-Whitney test [frequency], two-tailed Student's t-test [amplitude]). **f** Experimental scheme for measuring mEPSCs and sEPSCs in dentate gyrus interneurons (DG-INs) from vHPC of *Ptprd-meB*$^{+/-}$ mice (P56–70; male). **g** mEPSC frequencies and amplitudes in DG-INs from WT and *Ptprd-meB*$^{+/-}$ mice (P56–70; male). (n = 16, 5 [WT], 17, 6 [HT], two-tailed Mann–Whitney test, Frequency P = 0.0285). **h** sEPSC frequencies and amplitudes in DG-INs from WT and *Ptprd-meB*$^{+/-}$ mice (P56–70; male). (n = 16, 6 [WT], 18, 7 [HT], two-tailed Mann-Whitney test [frequency], two-tailed Student's t-test [amplitude]). Data values represent means ± SEM. Significance is indicated as *(<0.05), **(<0.01), or ns (not significant). Source data are provided as a Source Data file.

mEPSC frequency in DG-GCs, the mEPSC frequency (not amplitude) was increased (Fig. 2f, g). sEPSCs in *Ptprd-meB*$^{+/-}$ DG-INs were not altered, as seen for DG-GCs (Fig. 2h).

These results suggest that PTPδ-meB deletion leads to opposite changes of excitatory synaptic transmission in DG-GCs (decreased mEPSC frequency) versus DG-INs (increased mEPSC frequency) without affecting inhibitory synaptic transmission. Moreover, unlike the situation under PTPδ-meB deletion, PTPδ-meA deletion has minimal effects on mEPSCs in DG-GCs.

Opposite changes in excitatory synaptic density of *Ptprd-meB*$^{+/-}$ DG-GCs and DG-INs

The opposite changes seen in the mEPSC frequencies of *Ptprd-meB*$^{+/-}$ DG-GCs and DG-INs may involve alterations in excitatory synaptic

density or presynaptic release. To explore these possibilities, we performed electron microscopic (EM) analyses of excitatory synapses in DG-GCs and DG-INs. Among the various DG-IN types, we focused on parvalbumin (PV)-positive interneurons because they are a major source of synaptic inhibition and play a key role in mediating synaptic plasticity in DG granule cells, in contrast to somatostatin (SST)-positive interneurons[89–93]. Moreover, since SST-positive neurons have their cell bodies and dendrites in the DG hilus while their axons are confined to the molecular layer[91], it is unlikely that PTPδ-tdTomato-positive EC axons regulate these cells. We did not examine mossy cells—a critical regulator of DG granule cells[94]—because their axons mainly project to the inner molecular layer, an area where PTPδ-tdTomato signals are largely absent (Supplementary Fig. 4c), although a few exceptional cases may exist[95].

EM analyses of excitatory synapses on *Ptprd-meB*$^{+/-}$ DG-GCs, which were identified by the presence of the postsynaptic density (PSD) structures apposed to presynaptic axon terminals, indicated that the PSD density (number of spines per 1000 μm^2) was decreased in *Ptprd-meB*$^{+/-}$ mice, whereas the morphological parameters of PSDs (length, thickness, and perforation [a measure of synaptic maturation]) were unchanged (Fig. 3a–e).

Examination of excitatory synapses on *Ptprd-meB*$^{+/-}$ DG-INs, which were identified by VGLUT1-positive presynaptic structures localized on PV-positive dendrites apposed to axon terminals, revealed that the excitatory synaptic density was increased in mutant DG-INs (Fig. 3f, g), which contrasted with the decreased PSD density seen in *Ptprd-meB*$^{+/-}$ DG-GCs. We did not analyze the PSD morphology of DG-INs because identifying these structures in electron microscopic double-immunostained sections proved unreliable.

We hypothesized that the opposite changes seen in the densities of excitatory synapses on *Ptprd-meB*$^{+/-}$ DG-GCs and DG-INs could involve a differential presence of PTPδ proteins at the nerve terminals. We previously detected PTPδ-tdTomato signals in the nerve terminals apposed to excitatory synaptic PSD structures in the dorsal hippocampal CA1 region of juvenile mice[45]. It remained unknown in adult mice whether PTPδ-tdTomato signals are detected in the ventral hippocampal DG region and whether PTPδ-tdTomato signals are present at excitatory synapses on DG-INs in addition to DG-GCs. In the present study, our EM analysis revealed that presynaptic PTPδ-tdTomato signals could be detected in presynaptic nerve terminals of the ventral DG region and also at excitatory synapses of DG-GCs and DG-INs (PV-positive) in adult mice (Fig. 3h, i). Additionally, PTPδ-tdTomato signals were stronger in presynaptic regions than in postsynaptic areas, suggesting that these signals represent PTPδ expressed in EC neurons rather than DG neurons, as supported by the weak PTPδ-tdTomato signals observed in the granule cell layer and mossy fiber tracts originating from DG-GCs (Supplementary Fig. 4c).

These results collectively suggest that PTPδ-meB deletion leads to opposite changes in the density of excitatory synapses on DG-GCs and DG-INs (decreases and increases, respectively) in the ventral hippocampal DG region, suggesting that these changes may underlie the decreased and increased excitatory synaptic transmissions of DG-GCs and DG-INs, respectively. The presence of PTPδ-tdTomato signals in the nerve terminals of PV-positive DG-INs further suggests that presynaptic PTPδ may contribute to the opposite changes seen in excitatory synapses of DG-GCs and DG-INs.

Decreased excitatory/inhibitory synapse ratios in *Ptprd-meB*$^{+/-}$ DG-GCs

The opposite changes in excitatory synaptic transmission and density in *Ptprd-meB*$^{+/-}$ DG-GCs versus DG-INs suggest that excitatory synaptic input onto DG-GCs is decreased while inhibitory synaptic input from DG-INs onto DG-GCs is increased, which would decrease excitatory/inhibitory synaptic ratios in DG-GCs. To test this idea, we activated the medial EC-DG (MEC-DG) pathway by electrical or optogenetic stimulations and measured the ratios of evoked excitatory and inhibitory synaptic currents in DG-GCs.

When the MEC-DG pathway was electrically stimulated, the ratio of evoked EPSCs to IPSCs (eEPSC/eIPSC ratio) was reduced in *Ptprd-meB*$^{+/-}$ DG-GCs (Fig. 4a, b). For optogenetic stimulation, MEC neurons were infected with AAV9-hSyn-hChR2 (H134R)-mCherry and MEC terminals in DG-GCs in the middle molecular layer of DG were stimulated by blue light using a patterned illuminator (Supplementary Fig. 5b). The ratio of optogenetic EPSCs and IPSCs (oEPSC/oIPSC ratio) was similarly reduced in *Ptprd-meB*$^{+/-}$ DG-GCs (Fig. 4c, d). Intriguingly, the ratio of NMDA and AMPA receptor-mediated oEPSCs was not changed (Fig. 4e), suggesting that NMDA receptor EPSCs may be decreased along with AMPA receptor EPSCs.

The decreased oEPSC/oIPSC ratios in *Ptprd-meB*$^{+/-}$ DG-GCs might involve changes in neuronal excitability or the paired-pulse ratio (PPR; related to presynaptic release) in DG-GCs or DG-INs. Our results revealed that neuronal excitability was not changed in *Ptprd-meB*$^{+/-}$ DG-GCs or DG-INs, as shown by current-firing curves (Supplementary Fig. 6a, b). The PPR was decreased in the MEC-DG-GC pathway and increased in the DG-IN-GC pathway, while the MEC-DG-IN pathway showed normal in PPR (Supplementary Fig. 6c–e). We speculate that these alterations may represent compensatory changes, wherein presynaptic release at the MEC-DG-GC synapse increases to compensate for the decreased oEPSC/oIPSC ratio in *Ptprd-meB*$^{+/-}$ DG-GCs (see Discussion). When the lateral EC (LEC)-DG pathway was stimulated, oEPSC/oIPSC ratios remained unchanged in *Ptprd-meB*$^{+/-}$ DG-GCs (Supplementary Fig. 6f), in contrast to the reduced ratios observed in the MEC-DG pathway, highlighting distinct roles for PTPδ-meB in MEC-DG and LEC-DG pathways, in line with their distinct functions[96,97]. When oEPSC/oIPSC ratios were measured in *Ptprd-meA*$^{+/-}$ (not *Ptprd-meB*$^{+/-}$) DG-GCs, the ratio was increased (Fig. 4f). This sharply contrasts with the decreased oEPSC/oIPSC ratio in the *Ptprd-meB*$^{+/-}$ DG-GCs in the MEC-DG pathway, although it is in line with the increasing tendency of mEPSC frequency observed in *Ptprd-meA*$^{+/-}$ DG-GCs (Fig. 2e).

The decreased oEPSC/oIPSC ratios in *Ptprd-meB*$^{+/-}$ DG-GCs could involve the accumulation of excitatory synaptic changes in these neurons during embryonic and postnatal brain development. To exclude this possibility, we deleted PTPδ-meB from the young adult mouse brain (P35-40) by AAV-dependent Cre expression in MEC neurons of *Ptprd-meB*$^{+/flt}$ mice with floxed PTPδ-meB exons (Fig. 4g, h; Supplementary Fig. 5c). This decreased eEPSC/eIPSC ratios in DG-GCs, whereas, in a control experiment without Cre expression, eEPSC/eIPSC ratios were normal in DG-GCs (Fig. 4i).

These results suggest that PTPδ-meB deletion decreases the ratio of evoked excitatory and inhibitory synaptic transmissions in DG-GCs, whereas PTPδ-meA deletion leads to the opposite change (increased ratio of evoked excitatory and inhibitory synaptic transmissions). Moreover, the synaptic changes observed following PTPδ-meB deletion in the young adult brain suggest that these effects stem from an acute, presynaptic loss of PTPδ-meB.

Decreased excitatory synaptic levels of IL1RAP in *Ptprd-meB*$^{+/-}$ mice

We hypothesized that the decreased excitatory synaptic density in *Ptprd-meB*$^{+/-}$ DG-GCs could involve known binding partner(s) of PTPδ that require meB for trans-synaptic adhesion, such as IL1RAP, SALM3/5 (Lrfn4/5), and/or Slitrks[12–21]. If this were the case, the postsynaptic levels of some of these proteins could be reduced by PTPδ-meB deletion. To test this hypothesis in an unbiased manner, we undertook total proteomic analyses of synaptic proteins differentially enriched in the PSD and synaptic plasma membrane (SPM) fractions obtained from whole-brain lysates of WT and *Ptprd-meB*$^{+/-}$ mice (Fig. 5a).

We observed a significant decrease in the whole-brain level of the PTPδ-meB's trans-synaptic partner, IL1RAP[16], in the PSD fraction but not in the SPM fraction or whole lysates (Fig. 5b–d;

https://doi.org/10.1038/s41467-025-59685-3

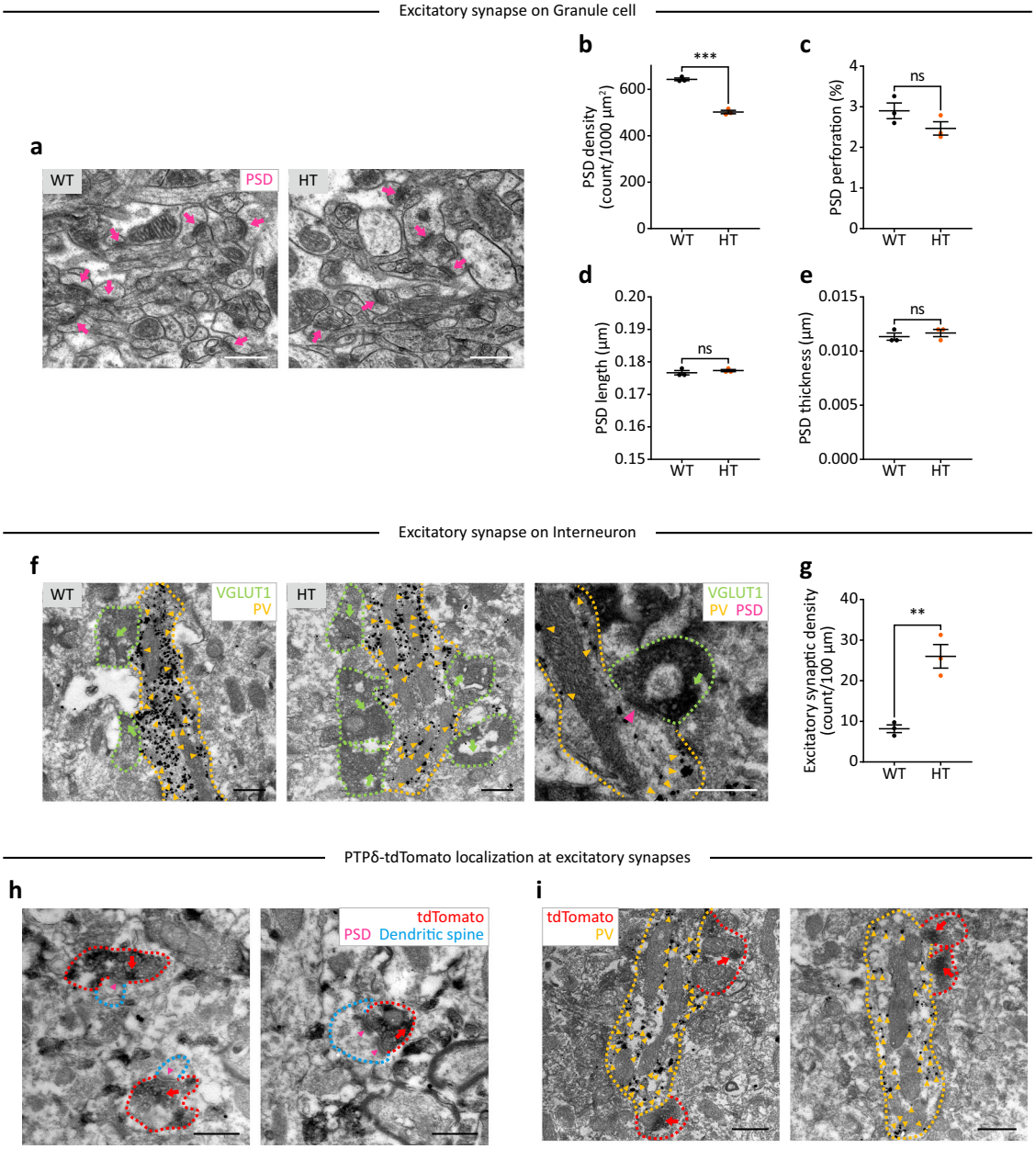

Fig. 3 | Opposite changes are seen in the excitatory synaptic densities of *Ptprd-meB*$^{+/-}$ DG-GCs and DG-INs. a Electron microscopic (EM) images of excitatory synapses on DG-GCs, marked by presynaptic axon terminals apposed to electron-dense postsynaptic density (PSD) structures (arrows) in dendritic spines (ventral dentate gyrus middle molecular layer) in WT and *Ptprd-meB*$^{+/-}$ (HT) mice (P63; male). Scale bar, 500 nm. **b**–**e** Quantification of PSD density and morphology (length, thickness, and perforation [a measure of synaptic maturation]) in WT and *Ptprd-meB*$^{+/-}$ mice (P63; male). ($n = 3$ mice [WT], 3 [HT], two-tailed Student's t-test, PSD density $P < 0.001$). **f** EM images of excitatory synapses on parvalbumin (PV)-positive DG-INs, identified by the presence of VGLUT1-positive presynaptic axon terminals (green arrows) apposed to PV-positive dendrites (yellow arrowheads; ventral dentate gyrus middle molecular layer) in WT and *Ptprd-meB*$^{+/-}$ mice (P63; male). An electron micrograph on the far right shows a large postsynaptic density (magenta arrowhead) at the synapse between a PV-positive dendrite (yellow arrowheads) and a VGLUT1-positive axon terminal (green arrow). Scale bar, 500 nm. **g** Quantification of excitatory synaptic densities in DG-INs (PV-positive interneurons) of WT and *Ptprd-meB*$^{+/-}$ mice (P63; male), as shown by excitatory synaptic density (count/100 µm). ($n = 3$ [WT], 3 [HT], two-tailed Student's *t*-test, $P = 0.0043$). **h**, **i** Detection of PTPδ-tdTomato fusion-protein signals (red arrows) in presynaptic nerve terminals (red dotted lines) apposed to dendritic spines (blue dotted lines) that include PSD structures (magenta arrowheads) and to PV-positive dendrites (yellow arrowheads) in the ventral DG region (middle molecular layer) of PTPδ-tdTomato reporter mice (P63; male). ($n = 4$ independent experiments using 4 PTPδ-tdTomato reporter mice for **h** and **i**). Scale bar, 500 nm. Data values represent means ± SEM. Significance is indicated as **(<0.01), ***(<0.001), or ns (not significant). Source data are provided as a Source Data file.

Supplementary Fig. 7; Supplementary Data 2). This finding indicates that IL1RAP was disproportionately lost from the PSD, although changes at specific cell types could be masked by pooling samples from various brain regions.

IL1RAP and 21 other PSD proteins with significant changes ($P < 0.05$ + |fold-change/FC| > 1.2; 13 upregulated and 9 downregulated) were enriched for the gene ontology/GO terms associated with synaptic functions ('synaptic vesicle' in KEGG and 'synapse' in the GO-CC/cellular component; DAVID analyses) (Fig. 5e). In SynGO analyses, ~45–50% of the 22 PSD proteins belonged to SynGO proteins: Presynaptic SynGO proteins were more frequent than postsynaptic SynGO proteins (SynGO: location), and the enriched synaptic

https://doi.org/10.1038/s41467-025-59685-3

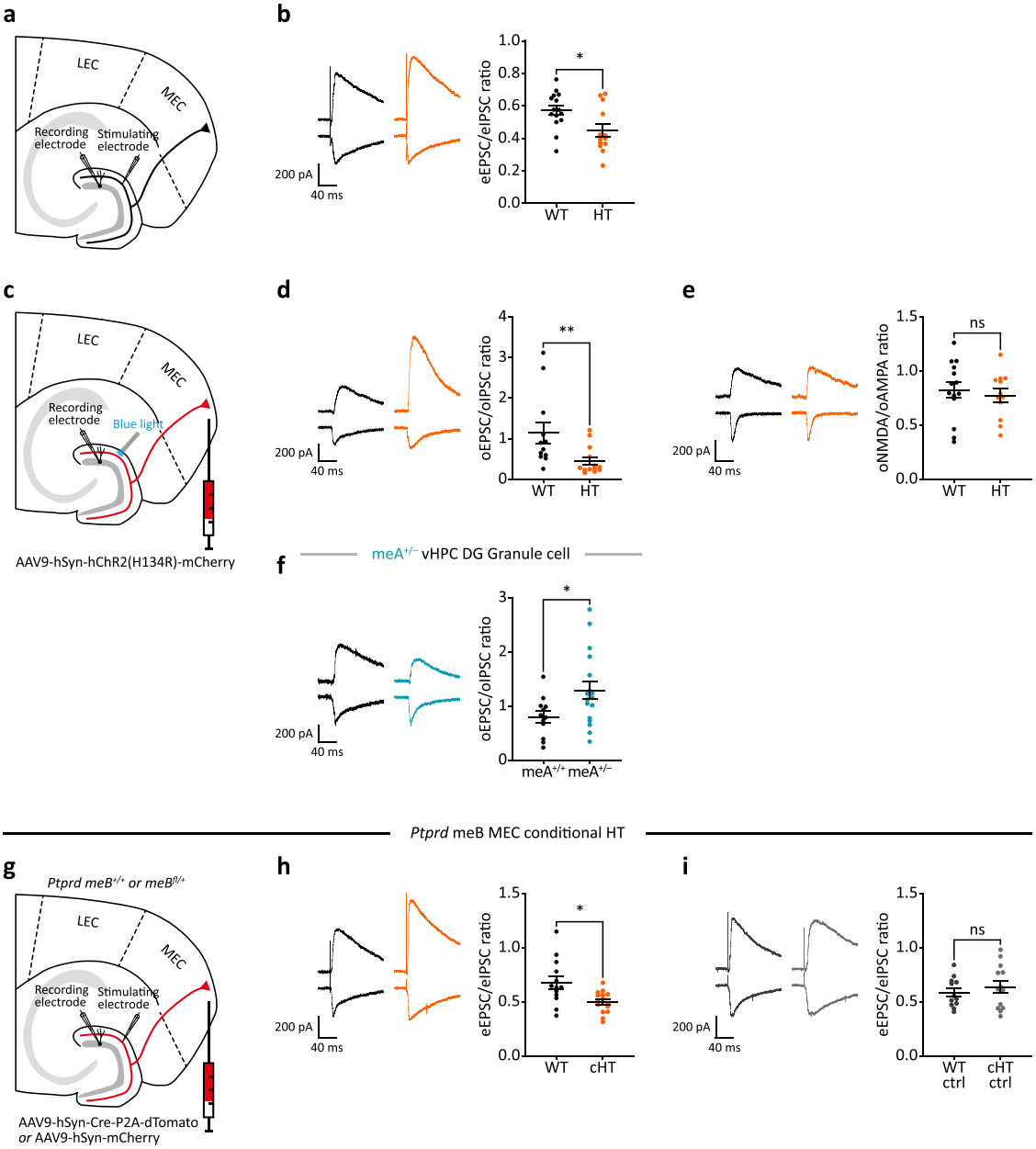

Fig. 4 | Ratios of excitatory to inhibitory synaptic transmissions are decreased in *Ptprd-meB*$^{+/-}$ DG-GCs. a Diagram showing electrical stimulation of the medial perforant pathway (MPP) originating from the medial entorhinal cortex (MEC), which was used to measure the ratio of electrically evoked EPSCs and IPSCs (eEPSC/eIPSC ratio). **b** Decreased eEPSC/eIPSC ratios in DG-GCs in the MEC-DG-GC pathway in *Ptprd-meB*$^{+/-}$ mice (P56–70; male). ($n = 15$ neurons from 3 mice [WT], 13, 3 [HT], two-tailed Student's *t*-test, $P = 0.0137$). **c** Diagram showing AAV-dependent expression of ChR2 in the MEC (AAV9-hSyn-hChR2[H134R]-mCherry; P35–40) and excitation of ChR2 in the middle molecular layer of the dentate gyrus (DG) region using a patterned illuminator, which was used to measure the ratio of optogenetically evoked EPSCs and IPSCs (oEPSC/oIPSC ratio). **d** Decreased oEPSC/oIPSC ratios in DG-GCs in the MEC-DG-GC pathway (MEC-DG-GCs) in *Ptprd-meB*$^{+/-}$ mice (P56–70; male). ($n = 12, 5$ [WT], 13, 4 [HT], two-tailed Mann-Whitney test, $P = 0.0066$). **e** Normal optogenetically evoked oNMDA-EPSC/oAMPA-EPSC ratios in MEC-DG-GCs in *Ptprd-meB*$^{+/-}$ mice (P56–70; male). ($n = 14, 3$ [WT], 12, 3 [HT], two-tailed Student's *t*-test). **f** Increased oEPSC/oIPSC ratios in MEC-DG-GCs in *Ptprd-meA*$^{+/-}$ mice (P56–70; male). ($n = 12, 3$ [meA$^{+/+}$], 17, 3 [meA$^{+/-}$], two-tailed Welch's *t*-test, $P = 0.0197$). **g** Diagram showing acute PTPδ-meB knockout in the young adult mouse brain by injecting AAV9-hSyn-Cre-P2A-dTomato into the MEC of WT and *Ptprd-meB*$^{+/fl}$ mice (P35–40) and measuring eEPSC/eIPSC ratios in MEC-DG-GCs (P70–75). AAV9-hSyn-mCherry was used as the control virus. **h** Decreased eEPSC/eIPSC ratios in MEC-DG-GCs in *Ptprd-meB*$^{+/fl}$ mice (P70–75; male) expressing Cre (cHT) in the medial EC. WT mice injected with AAV9-hSyn-Cre-P2A-dTomato were used as controls (WT). ($n = 13, 3$ [WT], 15, 3 [cHT], two-tailed Welch's *t*-test, $P = 0.0120$). **i** Unaltered eEPSC/eIPSC ratios in MEC-DG-GCs in *Ptprd-meB*$^{+/fl}$ mice (P70–75; male) injected with AAV9-hSyn-mCherry (cHT ctrl). WT mice injected with AAV9-hSyn-mCherry were used as controls (WT ctrl). ($n = 12, 3$ [WT ctrl], 13, 3 [cHT ctrl], two-tailed Student's *t*-test). Data values represent means ± SEM. Significance is indicated as *(<0.05), **(<0.01), or ns (not significant). Source data are provided as a Source Data file.

functions were 'synaptic vesicle', 'synaptic organization', and 'synaptic metabolism' (SynGO: function) (Fig. 5f, g).

Specifically, the identified SynGO proteins included synaptic vesicle-regulatory proteins (EXOC2, ATP6V1B2, and AP2A1), GAD1 (GABA-synthesizing enzyme), SEPTIN3 (presynaptic GTPase), MADD (Rab-GEF/guanine nucleotide exchanger), DOCK10 (spine-regulatory Cdc42-GEF), CAPN2 (calcium-activated protease), and RPS5 (ribosomal protein).

https://doi.org/10.1038/s41467-025-59685-3

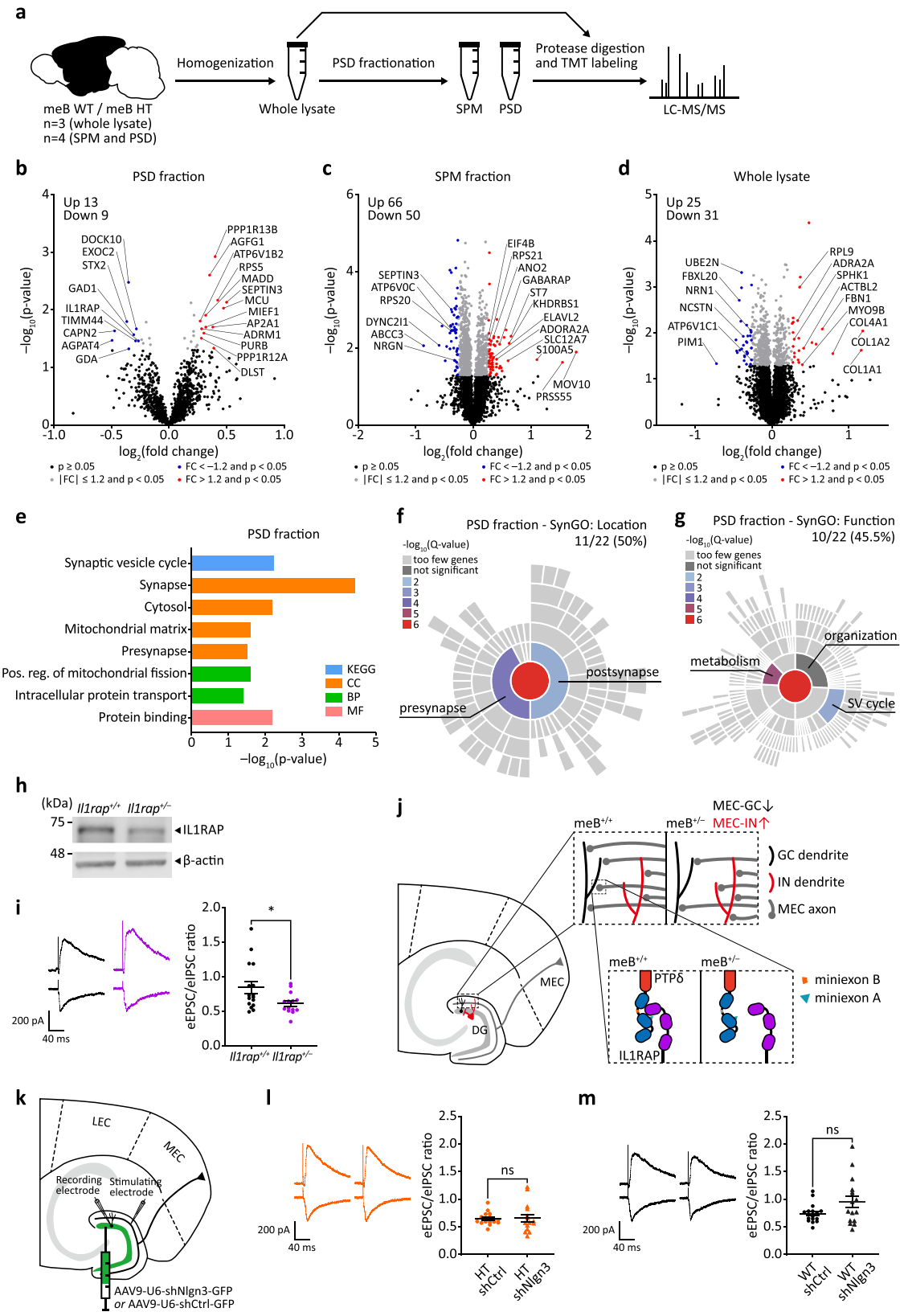

Given the possibility that the decreased PSD levels of IL1RAP may underlie the decreased excitatory synaptic density in *Ptprd-meB*$^{+/-}$ DG-GCs, we characterized heterozygous IL1RAP-mutant (*Il1rap*$^{+/-}$) mice to examine excitatory/inhibitory synaptic ratios in DG-GCs. Indeed, eEPSC/eIPSC ratios were decreased at *Il1rap*$^{+/-}$ MEC-DG-GC synapses in the ventral hippocampus (Fig. 5h, i), similar to the results obtained in *Ptprd-meB*$^{+/-}$ mice (Fig. 4a, b). These results suggest that PTPδ-meB deletion at the presynaptic side of *Ptprd-meB*$^{+/-}$ MEC-GC synapses reduces the postsynaptic levels of IL1RAP in the PSD of DG-GCs but not DG-INs, and thus selectively reduces the density of excitatory synapses in DG-GCs (Fig. 5j).

Fig. 5 | Decreased excitatory postsynaptic density levels of IL1RAP in *Ptprd-meB*$^{+/-}$ mice. a Diagram showing the total proteomic analyses of postsynaptic density (PSD) fractions, synaptic plasma membrane (SPM) fractions, and whole lysates from mice. **b**–**d** Volcano plots showing differentially expressed proteins (DEPs; $P < 0.05$ and |fold-change (FC)| >1.2) in *Ptprd-meB*$^{+/-}$ PSD, SPM, and whole lysate samples (P63; male; whole brain). ($n = 4$ mice [WT, HT] for PSD and SPM; 3 [WT, HT] for whole lysate, two-tailed Welch's *t*-test). **e** DAVID analyses of DEPs from *Ptprd-meB*$^{+/-}$ PSD samples. KEGG Kyoto Encyclopedia of Genes and Genomes, CC cellular component, BP biological process, MF molecular function. (Fisher's exact test). **f**, **g** SynGO analysis of DEPs from *Ptprd-meB*$^{+/-}$ PSD samples for pre/post-synaptic localization (SynGO: location) and synaptic functions (SynGO: function). **h** Western-blot validation of decreased IL1RAP protein levels in *Il1rap*$^{+/-}$ mice (P63; male). **i** Decreased eEPSCs/eIPSC ratios in DG-GCs in the MEC-DG-GC pathway in *Il1rap*$^{+/-}$ ventral hippocampus (P56–70; male). ($n = 16$ neurons from 4 mice [*Il1rap*$^{+/+}$], 14, 4 [*Il1rap*$^{+/-}$], two-tailed Mann–Whitney test, $P = 0.0344$). **j** A model suggesting that presynaptic PTPδ-meB deletion in the MEC decreases PSD levels of IL1RAP in DG-GCs (not DG-INs), thereby selectively decreasing excitatory synaptic density in DG-GCs. Note that whether the same axon provides excitatory synaptic inputs onto DG-GCs and DG-INs remains unknown. **k** Diagram showing acute *Neuroligin-3* (*Nlgn3*) knockdown by injecting AAV9-U6-shNlgn3-GFP into the ventral DG of mice (P35–40) and measuring eEPSC/eIPSC ratios in MEC-DG-GCs (P56–70). AAV9-U6-shCtrl-GFP, control virus. **l** Unaltered eEPSC/eIPSC ratios in MEC-DG-GCs in *Ptprd-meB*$^{+/-}$ mice (P56–70; male) injected with AAV9-U6-shNlgn3-GFP (HT shNlgn3). HT mice injected with AAV9-U6-shCtrl-GFP were used as controls (HT shCtrl). ($n = 18$, 3 [HT shCtrl], 15, 4 [HT shNlgn3], two-tailed Mann-Whitney test). **m** Unaltered eEPSC/eIPSC ratios in MEC-DG-GCs in WT mice (P56–70; male) injected with AAV9-U6-shNlgn3-GFP (WT shNlgn3). WT mice injected with AAV9-U6-shCtrl-GFP were used as controls (WT shCtrl). ($n = 18$, 4 [WT shCtrl], 16, 3 [WT shNlgn3], two-tailed Mann–Whitney test). Data values represent means ± SEM.

We next questioned why excitatory synaptic transmission and density were increased in *Ptprd-meB*$^{+/-}$ DG-INs and speculated that the relative abundance of IL1RAP might differ between the two post-synaptic DG neurons. Indeed, our analysis of single-nucleus RNA data from the Broad Institute Single Cell Portal[98,99] and MERFISH data from the Allen Brain Atlas[100,101] indicated that *Il1rap* mRNAs are strongly expressed in DG-GCs but minimally expressed in DG-INs of the mouse brain (Supplementary Fig. 8).

Additionally, PTPδ-meB deletion at excitatory presynaptic sites on DG-INs might enhance the trans-synaptic interaction between PTPδ and postsynaptic Neuroligin-3—a binding event that is promoted in the absence of meB[11]. If this were the case, reducing Neuroligin-3 expression in DG-INs should dampen the increase in excitatory PSD density and help restore normal eEPSC/eIPSC ratios in DG-GCs. To test this possibility, we knocked down Neuroligin-3 expression by infecting the DG region with AAV-U6-shNlgn3-GFP[102] and measured eEPSC/eIPSC ratios in DG-GCs. However, we observed no changes in these ratios in either WT or *Ptprd-meB*$^{+/-}$ shNlgn3-treated DG-GCs, although the baseline difference (decreased eEPSC/eIPSC ratios in mutant neurons) could be reproduced in this context (Fig. 5k–m; Supplementary Fig. 9). This finding suggests that increased trans-synaptic PTPδ-Neuroligin-3 interaction at DG-IN excitatory synapses is unlikely to underlie the altered eEPSC/eIPSC ratios in DG-GCs, although we cannot exclude the possibility that the remaining half of the Neuroligin-3 protein, which escaped knockdown, contributes to the increase in excitatory PSD density in DG-INs of *Ptprd-meB*$^{+/-}$ mice. AAV-U6-shNlgn3-GFP, however, may suppress Neuroligin-3 expression in DG-GCs in addition to DG-INs, although it could only decrease eEPSC/eIPSC ratios further in DG-GCs rather than rescuing it. Specific Neuroligin-3 knockdown in DG-INs driven by the mDlx enhancer was not attempted because validation of Neuroligin-3 knockdown in DG-INs by biochemical/immunohistochemical methods are likely to be unreliable.

Phospho-tyrosine proteomic analysis in *Ptprd-meB*$^{+/-}$ mice

PTPδ has a tyrosine phosphatase activity, and the deletion of PTPδ-meB and resulting alteration of presynaptic clustering of PTPδ may change tyrosine phosphorylation (pTyr) of synaptic proteins. In addition, our previous report on the analysis of global *Ptprd*$^{-/-}$mice indicated that PTPδ deletion leads to both synaptic loss of IL1RAPL1 and substantial decreases in the pTyr levels of IL1RAPL1 and other post-synaptic proteins[45], suggesting that these changes may collectively contribute to the decreased excitatory synaptic transmission observed in distal CA1 dendrites receiving EC inputs[45]. To this end, we undertook a proteomic analysis of pTyr levels using whole brains of *Ptprd-meB*$^{+/-}$ mice (Fig. 6a). Given that PTPδ-meB inclusion is observed in both excitatory and inhibitory neurons[49], we also analyzed pTyr patterns in mice with selective PTPδ-meB deletion in excitatory and inhibitory neurons (*Emx1-Cre;Ptprd-meB*$^{fl/fl}$ and *Vgat-Cre;Ptprd-meB*$^{fl/fl}$ mice, respectively).

Volcano plots of pTyr-polypeptides from *Ptprd-meB*$^{+/-}$ brains revealed many polypeptides with significant pTyr up- and down-regulations (termed DEPPs for differentially expressed protein peptides; $P < 0.05$ and $|FC| > 1.5$) (Fig. 6b; Supplementary Data 3). We identified relatively few DEPPs from *Emx1-Cre;Ptprd-meB*$^{fl/fl}$ and *Vgat-Cre;Ptprd-meB*$^{fl/fl}$ mice, compared to *Ptprd-meB*$^{+/-}$ mice (Fig. 6c, d; Supplementary Data 3), indicating that global PTPδ-meB deletion has greater effects in this regard. These differences may result from variations in sampling regions, as *Ptprd-meB*$^{+/-}$ mice were sampled from the whole brain (excluding the cerebellum and olfactory bulb), while *Emx1-Cre* and *Vgat-Cre* models were sampled only from the cortex and hippocampus, leaving non-cortical/hippocampal neurons unaffected. Additionally, heterozygous deletion suppresses gene expression in both neuronal and non-neuronal cells[103], whereas *Emx1*- and *Vgat*-driven deletion affect only a subset of neurons, potentially contributing to the observed differences.

DAVID analysis of *Ptprd-meB*$^{+/-}$ DEPPs indicated enrichments for GO terms associated with 'glutamatergic synapse', 'postsynaptic density', 'synaptic transmission', and 'protein binding' (Fig. 6e). In contrast, DAVID analysis of *Emx1-Cre;Ptprd-meB*$^{fl/fl}$ DEPPs indicated moderate enrichments for 'axon' and 'myelin sheath'-related GO terms (Fig. 6f). In SynGO analyses, *Ptprd-meB*$^{+/-}$ DEPPs were strongly enriched for postsynaptic specialization/PSD/membrane proteins (SynGO: location) and postsynaptic transmitter-gated ion channels (SynGO: function), while *Emx1-Cre;Ptprd-meB*$^{fl/fl}$ DEPPs were minimally enriched (Fig. 6g-i).

The SynGO proteins that overlapped with *Ptprd-meB*$^{+/-}$ DEPPs included glutamate receptor subunits (NMDAR2A, NMDAR2C, GLUR3 [NMDA/AMPA receptor subunits]), SHISA6 (postsynaptic AMPA receptor-regulatory protein), CADM2 (SynCAM2 synaptic adhesion molecule), synaptic scaffolding proteins (SAPAP3, LRRC7/densin-180, EPB41L1, CTNND2/catenin delta-2, MYO5A/myosin 5a), MAPK14 (p38α), CYLD (deubiquitinase), presynaptic vesicle-regulatory proteins (SYT7/synaptotagmin 7, DNM1/dynamin 1, and ATP6AP1), and Kv1.4 (potassium channel) (Fig. 6b). *Emx1-Cre;Ptprd-meB*$^{fl/fl}$ DEPPs with SynGO overlap included those corresponding to SYT1/2 and synaptic scaffold proteins (IL1RAPL1 and MAP1A).

While characterizing the functional consequences of altered phosphorylations is complex, we examined whether the reduced tyrosine phosphorylation of p38α (encoded by *Mapk14* and regulates synaptic functions[104–106]) in *Ptprd-meB*$^{+/-}$ mice is related to the decreased PSD levels of IL1RAP. IL1RAP forms a complex with IL1R1 upon IL-1β binding to IL1R1 to promote downstream p38 activation[107]. We thus treated cultured WT and *Ptprd-meB*$^{+/-}$ hippocampal neurons with IL-1β and examined p38 activation. Intriguingly, p38 activation—monitored by p38 phosphorylation—was significantly increased in IL-1β-treated *Ptprd-meB*$^{+/-}$ neurons, as compared with untreated WT neurons (Supplementary Fig. 10a-c), suggesting that mutant neurons

https://doi.org/10.1038/s41467-025-59685-3

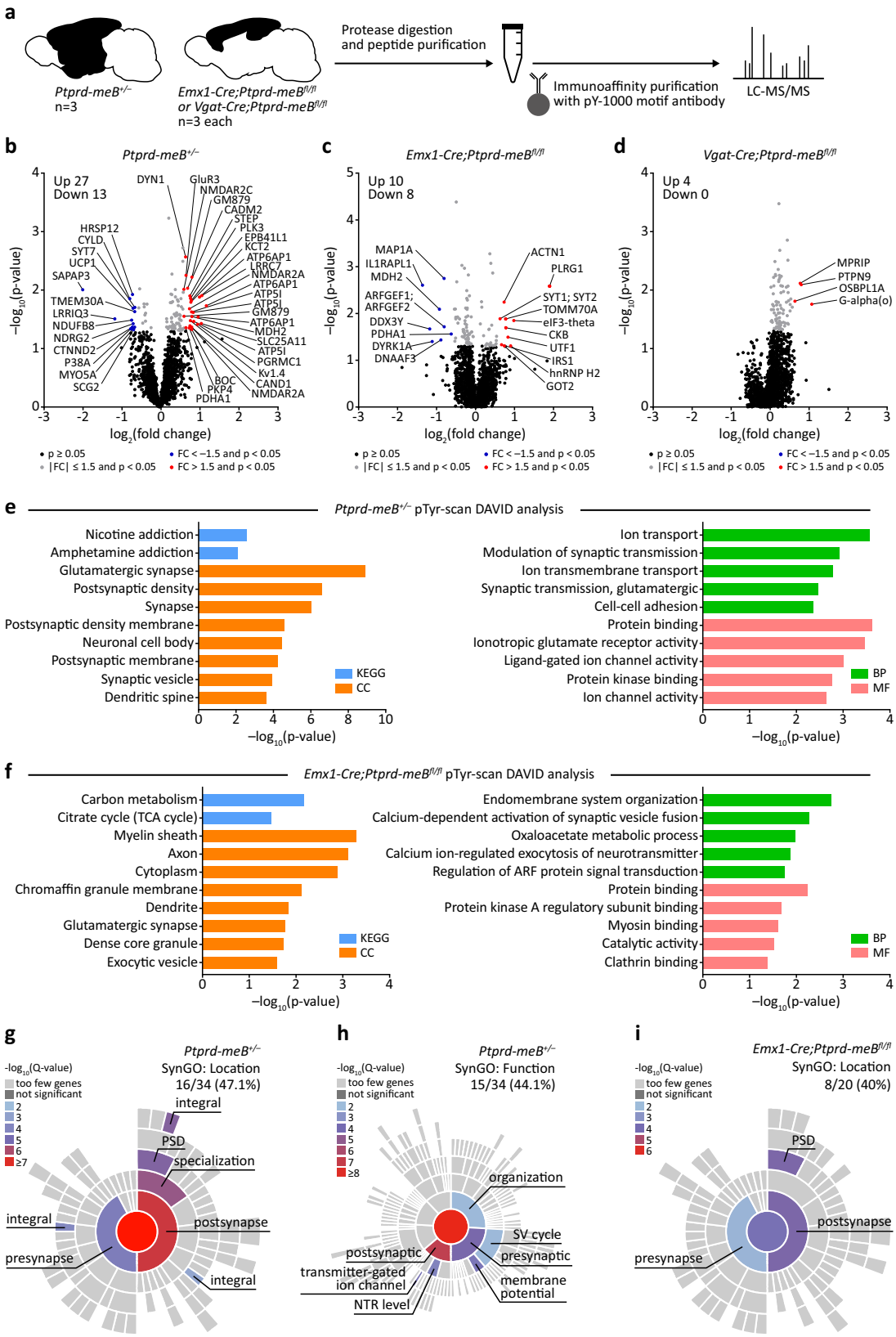

respond more strongly to IL-1β and that the trans-synaptic PTPδ-IL1RAP interaction may modulate postsynaptic IL-1β signaling (see Discussion).

These results collectively suggest that PTPδ-meB deletion in mice leads to substantial changes in pTyr levels of various synaptic proteins, including postsynaptic glutamate receptors and PSD scaffolding proteins, and their downstream signaling pathways, whereas presynaptic changes are relatively weak.

Discussion

The present study investigated in vivo functions of the meB splice insert of PTPδ in regulating early postnatal survival, excitatory synaptic

Fig. 6 | Phospho-tyrosine proteomic analysis in *Ptprd-meB*$^{+/-}$ mice. a Schematic of phospho-tyrosine (pTyr) proteomic analysis of whole-brain samples from *Ptprd-meB*$^{+/-}$, *Emx1-Cre;Ptprd-meB*$^{fl/fl}$ (excitatory neuron-specific; cortical and hippocampal regions), and *Vgat-Cre;Ptprd-meB*$^{fl/fl}$ (inhibitory neuron-specific; cortex and hippocampus regions) mice (P63; male). **b**–**d** Volcano plot of pTyr-DEPPs (for differentially expressed protein peptides; polypeptides with altered pTyr levels; $P < 0.05$ and $|FC| > 1.5$) from *Ptprd-meB*$^{+/-}$, *Emx1-Cre;Ptprd-meB*$^{fl/fl}$, and *Vgat-Cre;Ptprd-meB*$^{fl/fl}$ mice. ($n = 3$ mice [WT (*Ptprd-meB*$^{+/+}$), HT (*Ptprd-meB*$^{+/-}$)], 3 [*Ptprd-meB*$^{fl/fl}$, *Emx1-Cre;Ptprd-meB*$^{fl/fl}$], 3 [*Ptprd-meB*$^{fl/fl}$, *Vgat-Cre;Ptprd-meB*$^{fl/fl}$], two-tailed Student's *t*-test). **e**, **f** DAVID analyses of pTyr-DEPPs from *Ptprd-meB*$^{+/-}$ and *Emx1-Cre;Ptprd-meB*$^{fl/fl}$ mice. DAVID analysis for *Vgat-Cre;Ptprd-meB*$^{fl/fl}$ mice did not reveal any significant enrichment. KEGG Kyoto Encyclopedia of Genes and Genomes, CC cellular component, BP biological process, MF molecular function. (Fisher's exact test). **g**–**i** SynGO analyses of pTyr-DEPPs from *Ptprd-meB*$^{+/-}$ (**g**, **h**) and and *Emx1-Cre;Ptprd-meB*$^{fl/fl}$ (**i**) mice. Source data are provided as a Source Data file.

density/transmission, and mouse behaviors. We also compared in vivo impacts of PTPδ-meB and PTPδ-meA deletions, and found that PTPδ-meB deletion leads to strong phenotypes, as compared with those induced by PTPδ-meA deletion. We employed unbiased total proteomic analyses to identify IL1RAP as a key meB-dependent trans-synaptic partner of PTPδ that mediates excitatory synaptic phenotypes, such that IL1RAP-mutant mice show decreased excitatory/inhibitory synaptic ratios.

A key finding of the current study is that homozygous PTPδ-meB deletion in mice leads to early postnatal lethality, as shown by the ~3-fold increase in homozygote lethality observed at P7 relative to that at E18 and ~2-fold increase in homozygote lethality at P7 relative to global *Ptprd*$^{-/-}$ mice at P7. PTPδ-meB is involved in various trans-synaptic adhesions, which are critical for the formation of neuronal synapses and development of neural circuits. Homozygous PTPδ-meB deletion may impair normal development of neuronal synapses, neural circuits, and brain functions that are critically required for the survival of newborn mice. This sharply contrasts with the normal survival of the mice with homozygous PTPδ-meA deletion. Previous studies showed that alternative splicing in synaptic adhesion molecules plays various roles in synapse development (i.e., trans-synaptic adhesion) and function (i.e., trans-synaptic control of postsynaptic receptors)[64–80,108,109]. However, to our knowledge, the present study is the first to show that alternative splicing in a synaptic adhesion molecule can critically impact early postnatal survival.

Regarding why PTPδ-meB deletion has a stronger impact on neonatal survival compared to global PTPδ deletion, one possibility is that global deletion may induce compensatory changes in related proteins—such as an increase in PTPσ, as previously reported in the global *Ptprd*$^{-/-}$ hippocampus[45]—whereas the selective deletion of the meB exon does not trigger such compensatory increases. Given that the meB-containing isoform is the predominant form of PTPδ in vivo[17,18,49], its deletion in neonates may specifically impair meB-dependent synapse formation that are essential functions such as feeding. Newborn mammals rely on properly formed brainstem and spinal circuits—for instance, those mediating suckling reflexes and controlling cranial nerve motor pools—to establish functional synapses shortly after birth. If PTPδ-meB is required for connecting these circuits (e.g., by promoting presynaptic differentiation onto motor neurons that innervate the jaw and tongue, or onto hypothalamic feeding centers), its absence could lead to failure of neonates to nurse, ultimately resulting in early postnatal death.

PTPδ-meB deletion leads to decreased excitatory synaptic density and transmission in DG-GCs. With regard to the underlying mechanisms, our data suggest that IL1RAP, a trans-synaptic partner of PTPδ, is more important than other meB-dependent postsynaptic partners (i.e., Slitrks and SALM3/5) or meA-dependent partner (i.e., IL1RAPL1). Supporting this possibility, our unbiased total proteomic analyses suggest that IL1RAP is lost from the PSD upon PTPδ-meB deletion. In addition, acute Cre-dependent conditional deletion of PTPδ-meB in the MEC of young adult mice decreases eEPSC/eIPSC ratios in DG-GCs. IL1RAP is a postsynaptic adhesion molecule that interacts with meB-containing PTPδ; it regulates excitatory synaptic density in the hippocampus[16] and has been implicated in brain diseases, including schizophrenia[110,111] and Alzheimer's disease[112,113]. Our pTyr proteomic analyses further indicate that pTyr levels in various pre- and postsynaptic proteins are altered, suggesting that these proteins may also contribute to the excitatory synaptic phenotype. In contrast and in line with other phenotypes associated with alteration of meB versus meA (changes in early postnatal survival and behaviors), meA deletion minimally affected excitatory synaptic transmission in DG-GCs.

An intriguing consequence of PTPδ-meB deletion is increased excitatory synaptic transmission in DG-INs, which sharply contrasts with the decreased excitatory synaptic density and transmission seen in DG-GCs. A possible reason for the contrast could be the strong difference in the *Il1rap* gene expression levels of DG-GCs and DG-INs (high and low, respectively). Decreased PTPδ-meB in presynaptic terminals on DG-INs might promote the trans-synaptic adhesion of meB-lacking PTPδ with postsynaptic Neuroligin 3 to enhance excitatory synapse development. However, our Neuroligin-3 knockdown in the mutant DG did not rescue eEPSC/eIPSC ratios in DG-GCs, suggesting that an increase in Neuroligin-3 interaction with meB-lacking PTPδ is unlikely to underlie the increased excitatory transmission in DG-INs. Alternatively, presynaptic proteins derived from the decreased excitatory synapses on DG-GCs might be ectopically translocated to excitatory synapses on DG-INs. Although additional details need to be determined, it is worth noting that PTPδ-meB deletion in EC axons can cause opposite excitatory synaptic changes in two different postsynaptic neurons (decreased and increased excitatory synaptic transmissions in DG-GCs and DG-INs, respectively), likely further decreasing DG-GC output function. It is possible that DG-GCs and DG-INs may be concomitantly and oppositely regulated by the same presynaptic PTPδ-meB, perhaps to enable more efficient regulation of the excitatory-to-inhibitory synaptic ratios in DG-GCs. A recent study on LAR-RPTPs demonstrated that PTPδ-meA deletion has circuit-specific differential impacts on hippocampal CA1 neurons receiving inputs from different brain regions[49]. Our study extends these findings by demonstrating that the axons from the same brain region could form (or not form) meB-dependent trans-synaptic contacts with two different postsynaptic neurons having differing postsynaptic molecular compositions, and thereby develop excitatory synapses with distinct properties.

Our pTyr proteomic analysis revealed that the differentially expressed peptides in *Ptprd-meB*$^{+/-}$ mice predominantly localize to postsynaptic compartments, despite PTPδ's primarily presynaptic distribution. This finding suggests that a disrupted trans-synaptic PTPδ–IL1RAP interaction may underlie the altered postsynaptic pTyr levels. To explore the physiological implications of these changes, we examined the p38 signaling cascade downstream of IL1RAP. IL1RAP is known to form a complex with IL1R1 upon binding of the proinflammatory cytokine IL-1β, thereby promoting activation of p38 MAP kinase signaling[107,114,115]. Activated p38 subsequently phosphorylates and activates MAPK-activated protein kinase 2/3 (MK2/3), which can depolymerize actin through LIMK1-mediated regulation of cofilin, leading to disruption of F-actin structures within excitatory synapses[116–119]. Supporting this mechanism, in vivo experiments demonstrated that local infusion of IL-1β into the hippocampus induces significant loss of dendritic spines on CA1 pyramidal neurons[120], thus linking immune activation directly to synaptic structural alterations. Our results here indicate that IL-1β treatment significantly enhanced p38 activation in *Ptprd-meB*$^{+/-}$ neurons, indicating increased IL-1β responsiveness. These results suggest that the trans-synaptic

PTPδ–IL1RAP interaction plays an important role in modulating postsynaptic IL-1β-dependent p38 signaling and excitatory synaptic structure, although these mechanisms are speculative at present and require further detailed investigation.

Lastly, it is relevant that PTPδ has been implicated in various neurological, psychiatric, and neurodevelopmental disorders[27], including ADHD[28–31], intellectual disability[32], restless leg syndrome[33–36], insomnia[37], addiction[38,39], bipolar disorder[40], obsessive-compulsive disorder[41,42], and anxiety[43], although the underlying pathological mechanisms remain largely unclear. Here, we found that PTPδ-meB deletion could lead to decreased excitatory synaptic density/transmission and excitatory/inhibitory synaptic ratios in DG-GCs. Although it remains to be determined whether these changes also occur in other brain regions and/or at multiple developmental stages, our results suggest that PTPδ-related brain disorders may involve impaired PTPδ-meB-dependent excitatory synaptic development and altered excitatory/inhibitory synaptic balance in postsynaptic neurons.

In conclusion, we herein report in vivo evidence suggesting that PTPδ-meB is important for survival, synaptic, and behavioral phenotypes and that PTPδ-meB regulates excitatory synapses through cell-type-specific and IL1RAP-dependent trans-synaptic interactions. These mechanisms may contribute to the pathophysiology of PTPδ-related brain disorders.

Methods

Animals

LoxP-flanked *Ptprd-meB* mutant mice were generated by Biocytogen via CRISPR/Cas9-mediated genome editing. sgRNAs were specifically designed to target regions flanking exon 18 (meB). Candidate guide RNAs for the 5′ end [TAGTACCTTAAAGCCCTTACAGG] and 3′ end [GGTGTGAGAGGAGGGCGACGGGG] were created using the CRISPR design tool (http:/crispr.mit.edu). The selected sgRNAs included 5′ sgRNA 1 [TAGGTACCTTAAAGCCCTTAC], 5′ sgRNA 2 [AAACGTAAGG GCTTTAAGGTA], 3′ sgRNA 1 [TAGGTGTGAGAGGAGGGCGACG], and 3′ sgRNA 2 [AAACCGTCGCCCTCCTCTCACA]. A gene-targeting vector with the target region (exon 18) flanked by LoxP sequences and two homology arms was employed to repair the double-strand breaks (DSBs) induced by the Cas9/sgRNA. Female C57BL/6 N mice and KM mouse strains served as embryo donors and pseudopregnant foster mothers, respectively. Various concentrations of Cas9 mRNA and sgRNA were mixed and injected into the cytoplasm of fertilized eggs at the one-cell stage. Following injection, the surviving zygotes were implanted into the oviducts of KM albino pseudopregnant females. The founder pups were then verified by screening of PCR products. F1 heterozygous mice were produced, and subsequent generations were crossed with C57BL/6 J mice for at least 10 generations to ensure genetic background consistency. Whole-body meB deletion (*Ptprd-meB*$^{+/-}$) mice were generated by injecting a purified hexa-histidine-TAT-NLS-Cre (HTNC) enzyme into two-cell-stage embryos carrying heterozygous LoxP-flanked alleles. This method facilitated the direct generation of *Ptprd-meB*$^{+/-}$ mice without having to outbreed to introduce genetically encoded Cre[121]. The resulting *Ptprd-meB*$^{+/-}$ male mice were mated with *Ptprd-meB*$^{+/+}$ (wild-type) female mice to obtain *Ptprd-meB*$^{+/+}$ and *Ptprd-meB*$^{+/-}$ offspring. To genotype the floxed and *Ptprd-meB*$^{+/-}$ mice, the following primers were used: meB_Forward [CCCCAACTCTTCCCATTTCTCACCC], meB_Reverse [AGGAAAGGA CCCGAAAGTCAACCTC], and meB_Mut [ACACCTTGAGCTTAGGAA TGGCTGT]. All three primers were used in a single reaction, which yielded the following bands: wild-type, 362 bp; floxed, 435 bp; knockout, 317 bp.

We crossed *Ptprd-meB*$^{fl/fl}$ male mice with *Emx1-Cre;Ptprd-meB*$^{fl/fl}$ female mice to produce littermate pairs of *Ptprd-meB*$^{fl/fl}$ (cWT) and *Emx1-Cre;Ptprd-meB*$^{fl/fl}$ (*Emx1*-cKO) mice. *Ptprd-meB*$^{fl/fl}$ male mice were crossed with *Vgat-Cre;Ptprd-meB*$^{fl/fl}$ female mice to produce littermate pairs of *Ptprd-meB*$^{fl/fl}$ (cWT) and *Vgat-Cre;Ptprd-meB*$^{fl/fl}$ (Vgat-cKO) mice.

The details of *Ptprd* $^{+/-}$, *Ptprd-meA*$^{+/-}$ mice, and PTPδ-tdTomato fusion reporter mice were previously documented[45]. To genotype the floxed and *Ptprd* $^{+/-}$ mice, following primers were used in a single reaction: Ptprd_Forward [GGACCTTGACCAAAACAACCC], Ptprd_Reverse [GAGGGAGTCTATCTCATAAAAGC], and Ptprd_Mut [GACTGT GCTCCACAACTCTG]. This reaction produced bands at 274 bp for wild type, 326 bp for floxed, and ~180 bp for knockout. To genotype the floxed and *Ptprd-meA*$^{+/-}$ mice, following primers were used in a single reaction: meA_Forward [TGTCTTAAAAGTCAAAGAATGACTCCCC], meA_Reverse [ATCACTGCTCGAGGACCTCTGGATA], and meA_Mut [GGCCCACACAGTAGCTGTGGCAATA]. This reaction produced bands at 323 bp for wild type, 396 bp for floxed, and 284 bp for knockout. For genotyping the PTPδ-tdTomato fusion reporter mice, the following primers were used: Tomato_Control_Forward [AAGCCTGTATTGGG TTGACTGGTGA] and Tomato_Control_Reverse [TGCCTCCTAAGTCA GGATTCTTGTT], which produced a wild type band of 529 bp. The primers Tomato_Mutant_Forward [TCCTGTACGGCATGGACGAGCT GTA] and Tomato_Mutant_Reverse [ACAGGCAAGCTCTCTCTGTCCC TAT] were used to generate a mutant band of 422 bp.

Il1rap$^{+/-}$ mice (The Jackson Laboratory, #003284), *Emx1-Cre* mice (The Jackson Laboratory, #005628), and *Vgat-Cre* mice (The Jackson Laboratory, #028862) were purchased from The Jackson Laboratory and genotyped according to the protocols provided by The Jackson Laboratory.

All mice used in this study are on a C57BL/6 J background. Mice were weaned between the ages of P21–28, and same-sex littermates of mixed genotypes were group-housed. Mice were fed *ad libitum* and housed under a 12 h light/dark cycle. All experiments, except for the identification of embryo/pup genotype ratios, were conducted using male mice aged P56 to P84. Embryo or pup genotype ratios were acquired from both male and female mice aged embryonic day (E) 18 or P7, respectively. All experimental procedures were approved by KAIST Institutional Animal Care and Use Committee (KA2023-071).

Immunoblot analysis

Whole brains, except olfactory bulb, cerebellum, and brainstem, were homogenized using motorized tissue grinder in ice-cold homogenization buffer (0.32 M sucrose, 10 mM HEPES containing protease and phosphatase inhibitors; buffered at pH 7.4). The whole lysates were used without any further fractionation. Cultured neurons were also harvested using ice-cold homogenization buffer by scraping with a cell scraper. Blots were imaged and analyzed using the Odyssey Fc Imager (Li-COR Biosciences) and Image Studio Lite 4.0 (Li-COR Biosciences). The following antibodies were generated using the indicated peptides: PTPδ N-term (home-made, #2063, IIQHKPKNSEEPY-KEIDGIATTRYSVAGLSPYSDYEFR), PTPδ C-term (home-made, #2061, RPAMVQTEDQYQFCYRAALEYLGSFDHYAT). The following antibodies were commercially purchased: β-actin (Sigma, A5316), IL1RAP (Cell Signaling, #52686), Neuroligin-3 (SYSY, 129 113), p38 (Cell Signaling, #9212), and phospho-p38 (Cell Signaling, #9211).

tdTomato imaging

Wild type or heterozygous PTPδ-tdTomato reporter mice (postnatal day 63; male) were transcardially perfused with 4% paraformaldehyde. Following overnight incubation (4 °C) in 4% paraformaldehyde, each mouse brain was sectioned horizontally at 50 μm using a Vibratome (Leica, VT1200S). Brain slices were mounted in Vectashield antifade mounting medium with DAPI (Vector Laboratories, H-1200). Images were acquired with a slide scanner (Carl Zeiss, Axio Scan. Z1) and a confocal microscope (Carl Zeiss, LSM 780). Image acquisition and analysis were performed using ZEN Microscopy Software (Carl Zeiss).

cDNA preparation and RT-qPCR

RNA was extracted from the whole brain (excluding olfactory bulb, cerebellum, and brainstem) of mice at postnatal day 63 (male) using

TRIzol™ (Thermo Fisher, 15596018). cDNA was then synthesized using the M-MLV cDNA Synthesis kit (Enzynomics, EZ006M), followed by real-time quantitative PCR (RT-qPCR) using THUNDERBIRD™ SYBR® qPCR Mix (TOYOBO, QPS-201) on a CFX96 Real-Time PCR System (Bio-Rad). *Gapdh* served as the reference gene. The efficiency of all RT-qPCR primers ranged from 95-105%.

The following primers were used:

For *Ptprd* miniexon B (exon 18) quantification: meB_qPCR_F [CAGAGAGCTGCGAGAAGTTC] and meB_qPCR_R [CCCACTGCCACACAGGTGATATTT].

For *Ptprd* miniexon A (exon 15 and 16) quantification: meA_qPCR_F [CGATCAGAATCTATTGGTGGTACACC] and meA_qPCR_R [CATATAAATTGGCAGGGGCAGAGTAG].

For *Ptprd* exon 13 quantification: E13_qPCR_F [CGATGGATCTGGATCAGTACTCAG] and E13_qPCR_R [CCCTCTAGGAATCTGATCCTCACG].

For *Gapdh* quantification: Gapdh_qPCR_F [TCAGCAATGCATCCTGCACCACC] and Gapdh_qPCR_R [TGGCAGTGATGGCATGGACTGTG].

Behavioral assays

Age-matched male or female mice (postnatal day 56–84) were used for behavioral tests during light-off periods. The mice were handled for three consecutive days (10 min/day) before behavioral tests. Mice were acclimated in a dark room >30 min before the behavioral test on the test date.

LABORAS

The Laboratory Animal Behavior Observation Registration and Analysis System (Metris, LABORAS™) was employed to track continuous movements of isolated mice for 96 h, without any researcher's interference. Mice that were previously housed in groups were individually placed in cages on a vibration-sensitive platform inside a sound-attenuated room. Data from the first 24 h, when the mouse is not fully familiarized with the environment, were not included in the analysis. Every 24 h period was divided into 3 h time bins and variables were averaged across corresponding time bins to represent a single 24 h period. Additionally, we measured the weight of the water, food, and each mouse before and after the recording. Data acquisition and analysis were conducted using LABORAS 2.6 software (Metris).

Open-field test

Mice were positioned in a white acrylic open-field box (40 × 40 × 40 cm), and their movements were recorded for 60 min. The lighting conditions were maintained at 0 lux. The distance moved and center (20 × 20 cm) time duration were analyzed using EthoVision XT 17 software (Noldus).

Elevated plus-maze test

Mice were positioned in the center of an elevated plus maze, featuring two open arms and two 30 cm-walled arms (each arm 5 × 30 cm). The maze was elevated 75 cm from the ground. Mice movements were recorded for 10 min. The lighting conditions of open arms were maintained at 200 lux. Time spent in each arm and the total distance moved were analyzed using EthoVision XT 17 software (Noldus).

Light-dark test

The light-dark box was made up of a white, open-roofed light chamber (20 × 30 × 20 cm) attached to a black, closed dark chamber (20 × 13 × 20 cm) with a small opening (8 × 8 cm) to enable unrestricted passage between the two chambers. Mice were placed in the center of a light chamber, and their movements were recorded for 10 min. The lighting conditions in the light chamber were maintained at 200 lux. An entry into the light chamber was counted only when the whole body of the subject moved through the opening. Time spent in the light chamber and the number of entries were analyzed using EthoVision XT 17 software (Noldus).

Acoustic startle response

Acoustic startle responses were measured using the SR-LAB startle response system (SD Instruments). The setup included an animal enclosure equipped with an attached sensor and a test cabinet that incorporated a sound generation system. Mice were placed in the animal enclosure, which was then positioned inside the test cabinet. To acclimate the mice, a background noise pulse of 65 dB was administered for 5 min. Following acclimation, 92 test sound pulses were delivered with inter trial intervals varying from 7–23 s. These test sound pulses were composed of 4 initial pulses of 40 ms at 120 dB, followed by 77 testing pulses (7 times each of 70, 75, 80, 85, 90, 95, 100, 105, 110, 115, and 120 dB, 40 ms), and concluding with 4 final pulses of 40 ms at 120 dB, along with 7 trials that emitted no sound. Startle responses to each test sound pulse were averaged across trials. The lighting conditions in the test cabinet were maintained at ~0 lux. The sensitivity of the sensor and the sound level were calibrated prior to the experiments using the SR-LAB standardization unit (SD Instruments) and a decibel meter, respectively.

Auditory brainstem response (ABR) and Distortion Product Otoacoustic Emissions (DPOAE)

All hearing analyses were performed under anesthesia using a mixture of Rompun (0.4 ml/kg) and Zoletil (0.6 ml/kg). ABRs were measured in a custom-made shielded soundproof chamber equipped with SmartEP (Intelligent hearing systems), which was fitted with high-frequency transducers (HFT9911-20-0035) and operated using high-frequency software version 5.10 (Intelligent Hearing Systems). Subdermal stainless-steel needle electrodes were placed at the vertex as the active electrode and below the non-tested pinna as the reference electrode. These were connected to a preamplifier (× 100,000), with a bandpass filter set from 0.1 to 1.5 kHz. The acoustic stimuli consisted of a click (100 μs in duration; 31 Hz) and tone bursts at 6, 12, 18, 24, and 30 kHz (1562 μs in duration; $\cos^2$-shaped; 21 Hz), which were presented to the tested ear canal through the test tube. The sound stimulus started at 90 dB SPL and was reduced in 10 dB increments to determine the threshold. The electrical responses obtained in the first 12 ms after the stimuli were averaged over 512 sweeps. Thresholds were defined as the lowest stimulus intensity at which typical waves could still be distinguishable. DPOAEs were recorded over the range of 6 to 32 kHz using an IHS Smart OAE 5.10 system. An Etymotic 10B+ probe was inserted into the external ear canal, working in conjunction with two transducers: the Etymotic ER2 stimulator for frequencies 6–14 kHz, and an IHS high-frequency transducer for frequencies 16–32 kHz. The L1 amplitude was set at 65 dB SPL, and the L2 amplitude at 55 dB SPL. Frequencies were acquired with an f1/f2 ratio of 1.22. A total of eight blocks were recorded, each consisting of 30 sweeps.

Pup retrieval test

Adult virgin female mice were isolated in the home-cages with Nestlets for 3 days before the pup retrieval test. On the day of the test, three pups (postnatal day 4) were placed in three corners of the home-cage. The retrieval behavior of the female mice was recorded for 10 min. The lighting conditions during the experiment were maintained at 50 lux. The time taken to retrieve each pup into the nest was manually analyzed. Female mice that retrieved pups outside the nest were excluded from the statistical analysis.

Brain slices for electrophysiology

Acute hippocampal-entorhinal cortex (HEC) brain slices were prepared from postnatal day 56–75 (adult) male mice that were anesthetized using isoflurane (Terrell). The brains were removed and immersed in a 0 °C dissection buffer containing, in mM: 75 sucrose, 76 NaCl, 25

$NaHCO_3$, 2.5 KCl, 1.25 NaH_2PO_4, 25 D-glucose, 7 $MgSO_4$, and 0.5 $CaCl_2$ (bubbled with 95% O_2 and 5% CO_2). The ventral hippocampus HEC slices, cut to 300 µm using a vibratome (Leica, VT1200S), were then placed in a holding chamber at 32 °C filled with dissection buffer. The slices underwent a recovery period at 32 °C for 25 min. The slices were then transferred to a holding chamber at room temperature (20-25 °C) containing artificial cerebrospinal fluid (aCSF; in mM: 124 NaCl, 26.2 $NaHCO_3$, 2.5 KCl, 1 NaH_2PO_4, 20 D-glucose, 1.3 $MgCl_2$, 2.5 $CaCl_2$; bubbled with 95% O_2 and 5% CO_2) and recovered for additional 30 min. Afterwards, they were moved to a recording chamber, where all electrophysiological experiments were carried out at 27–28 °C with a circulating aCSF solution. Neurons were visualized under differential interference contrast illumination in an upright microscope (B50WI, Olympus).

Whole-cell recording

For whole-cell patch clamp recordings, we used thin-walled borosilicate capillaries (Harvard Apparatus, 30-0065) to make pipettes with a resistance of 3.5–4.5 MΩ using a two-step vertical puller (Narishige, PC-10). Signals were filtered at 2 kHz and digitized at 10 kHz using the Multiclamp 700B Amplifier (Molecular Devices), Multiclamp Commander 700B software (Molecular Devices), the Digidata 1550 Digitizer (Molecular Devices), and pClamp 10.1 software (Molecular Devices). The cells were approached with a pipette filled with internal solution to make a gigaohm seal, followed by gentle rupture of the cells. After the cell membranes were ruptured, we allowed the cells to stabilize for at least 3 min before starting the recordings. Throughout this stabilization period, and just before and after recording, we monitored the access resistance, ensuring it did not exceed 20 MΩ; otherwise, the data were excluded from the analysis.

For recordings of mEPSC, sEPSC, optogenetically evoked EPSC/IPSC ratio (oEPSC/oIPSC ratio), electrically evoked EPSC/IPSC ratio (eEPSC/eIPSC ratio), NMDA/AMPA ratio, EPSC paired-pulse ratio (EPSC-PPR), and IPSC paired-pulse ratio (IPSC-PPR), pipettes were filled with an internal solution composed of, in mM, 130 $CsMeSO_4$, 10 TEA-Cl, 10 HEPES, 10 EGTA, 4 Mg-ATP, 0.3 Na-GTP, and 0.5 QX-314. For mEPSC experiments, 10 µM SR-95531 (Sigma) and 0.5 µM tetrodotoxin (Tocris) were added to the aCSF. For sEPSC experiments, 10 µM SR-95531 was added to the aCSF. Neurons were voltage-clamped at −70 mV for the recording of mEPSCs and sEPSCs.

To measure oEPSC/oIPSC ratio, NMDA/AMPA ratio, EPSC-PPR, and IPSC-PPR, blue-light (470 nm) LED illumination was applied for 5 ms at an intensity of 1–2 mW using a Digital Mirror Device-based pattern illuminator (Mightex, Polygon 1000) to activate neurons expressing channelrhodopsin-2 (ChR2). For medial perforant pathway (MPP) activations, the middle third of the molecular layer was specifically targeted.

oEPSC/oIPSC measurement was conducted in aCSF. DG granule cells were voltage-clamped at −70 mV, and oEPSCs were elicited using blue-light LED illumination. After oEPSC recording, the holding potential was shifted to 0 mV to record oIPSCs. Each type of postsynaptic current was recorded 15 sweeps. To assess the NMDA/AMPA ratio, the holding potential was alternated between −70 mV and +60 mV to separately measure AMPAR-mediated EPSCs and NMDAR-mediated EPSCs, respectively. Both EPSCs were triggered by blue-light LED illumination. The experiments were conducted in aCSF containing 10 µM SR-95531. NMDAR-mediated EPSCs was measured at 50 ms after the onset of stimulation. Measurements of EPSC-PPR and IPSC-PPR were performed in aCSF with the cells voltage-clamped at −70 mV and 0 mV, respectively. Paired LED illuminations were applied at intervals of 50, 100, 150, and 200 ms. The PPR for each interval was calculated by dividing the amplitude of the second peak by the amplitude of the first peak.

To measure eEPSC/eIPSC ratios, a brain slice in aCSF was electrically stimulated using a stimulus isolator (WPI, A365). The stimulating electrode was positioned in the middle third of the molecular layer to specifically target the MPP. To specifically target the lateral perforant path/LPP, the stimulating electrode was positioned in the outer third of the molecular layer, which is the part farthest from the granule cell layer when the molecular layer is evenly divided into three parts. Granule cells were voltage-clamped at −70 mV and 0 mV to measure eEPSC and eIPSC, respectively.

For mIPSC recordings, the internal solution contained, in mM, 135 KCl, 2 $MgCl_2$, 10 HEPES, 4 Na-ATP, 0.3 Na-GTP. In the mIPSC experiments, 10 µM NBQX (Tocris), 50 µM D-AP5 (Tocris), and 0.5 µM tetrodotoxin (Tocris) were added to the aCSF. The voltage was clamped at −70 mV.

For intrinsic excitability measurements, pipettes were filled with an internal solution containing, in mM, 135 K-gluconate, 7 NaCl, 10 HEPES, 0.5 EGTA, 2 Mg-ATP, 0.3 Na-GTP, and 10 phosphocreatine di(tris). This internal solution was also used for sEPSC recordings in interneurons, allowing consecutive recording of sEPSC and intrinsic excitability in a single neuron. Measurements of intrinsic excitability were conducted in current-clamp mode. Minimal currents were injected to maintain the membrane potential around −80 mV for granule cells and −70 mV for interneurons. To elicit sustained firing, increasing amounts of depolarizing step currents were injected.

All internal solutions were titrated to pH 7.3 and adjusted to the osmolarity of 295 mOsm. The acquired data were analyzed using Clampfit 10 (Molecular Devices) and Minhee Analysis Package[122].

Stereotaxic virus injection

Virus injections were performed on mice at the age of postnatal week 5. The virus was injected to either the ventral hippocampus dentate gyrus (coordinates: AP = −3.7; ML = ± 2.6; DV = −3.0) or the medial entorhinal cortex (coordinates: AP = −4.5; ML = ± 3.1; DV = −3.2) via stereotaxic surgery. Initially, mice were anesthetized with an intraperitoneally (IP) injected cocktail of ketamine (50 mg/ml, Yuhan) and xylazine (23.32 mg/ml, Elanco). The dosages for the IP injection were 100 mg/kg for ketamine and 8.3 mg/kg for xylazine. After mice were confirmed anesthetized, they were affixed onto the stereotaxic platform (Kopf Instruments, Model 940) and leveled at the bregma-lambda axis. Each virus was delivered to the target region using a 33 gauge NanoFil needle (WPI, NF33BL-2). The following viruses were purchased from Addgene: AAV9-mDlx-GFP-Fishell-1 (#83900-AAV9), AAV9-hSyn-hChR2(H134R)-mCherry (#26976-AAV9), AAV9-hSyn-Cre-P2A-dTomato (#107738-AAV9), AAV9-hSyn-mCherry (#114472-AAV9), AAV9-mDlx-ChR2-mCherry-Fishell-3 (#83898-AAV9). pAAV-U6-shNlgn3-GFP (5′-CCACTGAATTAAGTGTCACTA-3′) and pAAV-U6-shCtrl-GFP (5′-CAACAAGATGAAGAGCACCAA-3′) were subcloned in-house, and AAV9 packaging was conducted through the IBS Virus Facility. The sequence of shNlgn3 was obtained from a previous study[102].

Electron microscopy

For the quantification of excitatory synapse, three *Ptprd-meB*$^{+/+}$ and three *Ptprd-meB*$^{+/-}$ mice (postnatal day 63; male) were utilized. The mice were deeply anesthetized with a mixture of ketamine (120 mg/kg) and xylazine (10 mg/kg), followed by intracardial perfusion with 10 ml of heparinized normal saline and 50 ml of a freshly prepared fixative containing 2.5% glutaraldehyde and 1% paraformaldehyde in 0.1 M phosphate buffer (PB, pH 7.4). The hippocampus was dissected from the whole brain, post-fixed in the same fixative for 2 h, and then stored in 0.1 M PB at pH 7.4 overnight at 4 °C. Sections were cut transversely at 60 µm using a Vibratome. The sections underwent osmication with 1% osmium tetroxide (in 0.1 M PB) for 1 h, dehydration through a graded series of alcohols, flat embedding in Durcupan ACM (Fluka), and were cured for 48 h at 60 °C. Small pieces containing the middle molecular layer of the ventral hippocampal dentate gyrus were excised from the wafers and adhered to a plastic block using cyanoacrylate. Ultrathin sections were prepared and mounted on Formvar-coated

single-slot grids. The sections were stained with uranyl acetate and lead citrate. Subsequently, they were examined using an electron microscope (Hitachi H-7500; Hitachi) at an accelerating voltage of 80 kV. Digital images were captured using a GATAN DigitalMicrograph system with a CCD camera (SC1000 Orius; Gatan) and saved as TIFF files.

Electron microscopic immunochemistry

For double immunostaining of vesicular glutamate transporter 1 (VGLUT1) and parvalbumin (PV), three *Ptprd-meB*$^{+/+}$ and three *Ptprd-meB*$^{+/-}$ mice (postnatal day 63; male) were utilized. For double immunostaining of tdTomato and PV, four PTPδ-tdTomato fusion reporter mice (postnatal day 63; male) were used. The animals were deeply anesthetized with a mixture of ketamine (120 mg/kg) and xylazine (10 mg/kg) and intracardially perfused with 10 ml of heparinized normal saline followed by 50 ml of freshly prepared 4% paraformaldehyde and 0.01% glutaraldehyde in 0.1 M PB. The hippocampus was then extracted from the whole brain and postfixed in the same fixative for 2 h at 4 °C. Sections were cut transversely at 60 µm on a Vibratome and cryoprotected in 30% sucrose in PB overnight at 4 °C. The sections were then frozen on dry ice for 20 min and thawed in phosphate-buffered saline (PBS, 0.01 M, pH 7.4) to enhance penetration. Sections were pretreated with 1% sodium borohydride for 30 min to quench glutaraldehyde and then blocked with 3% H_2O_2 for 10 min to suppress endogenous peroxidases and with 10% normal donkey serum (NDS, Jackson ImmunoResearch, West Grove, PA, USA) for 30 min to mask secondary antibody binding sites. Overnight incubation was then performed with a mixture of primary antibodies: rabbit anti-PV (1:1000, PV 25, Swant, Burgdorf, Switzerland) and guinea pig anti-VGLUT1 (1:1000, 135-304, Synaptic Systems, Göttingen, Germany) or goat anti-tdTomato (1:600, AB8181-200, SICGEN, Cantanhede, Portugal). Following this, sections were rinsed in PBS for 15 min and incubated with a mixture of 1 nm gold-conjugated donkey anti-rabbit (1:50, EMS, Hatfield, PA, USA) and biotinylated donkey anti-guinea pig (1:200) or biotinylated donkey anti-goat (1:200) antibodies for 2 h. After postfixation with 1% glutaraldehyde in PBS for 10 min, sections were rinsed in PBS, incubated for 4 min with HQ silver enhancement solution (Nanoprobes, Yaphank, NY, USA), and then rinsed in 0.1 M sodium acetate and PBS. They were then incubated with ExtrAvidin peroxidase (1:5000, Sigma, St. Louis, MO, USA) for 1 h, and the immunoperoxidase was visualized using nickel-intensified 3,3′-diaminobenzidine tetrahydrochloride (DAB). Sections were further rinsed in PB, osmicated (in 0.5% osmium tetroxide in PB) for 30 min, dehydrated in graded alcohols, flat-embedded in Durcupan ACM (Fluka, Buchs, Switzerland) between strips of Aclar plastic film (EMS), and cured for 48 h at 60 °C. Chips containing prominent staining for VGLUT1/PV or tdTomato/PV in the middle molecular layer of the ventral hippocampal dentate gyrus regions were cut out of the wafers and glued onto blank resin blocks with cyanoacrylate. Serially cut thin sections were collected on Formvar-coated single-slot nickel grids and stained with uranyl acetate and lead citrate. Grids were examined on a Hitachi H7500 electron microscope (Hitachi, Tokyo, Japan) at 80 kV accelerating voltage. Digital images were captured with GATAN DigitalMicrograph software driving a CCD camera (SC1000 Orius; Gatan) and saved as TIFF files.

To control for specificity of PV, VGluT1 and tdToamto antibodies, we processed tissues according to the above protocols, except that primary antibodies were omitted; this completely abolished specific staining. The pattern of PV and VGluT1 immunostaining in the hippocampus was also similar to that in previous studies[123,124].

Quantitative analysis of electron microscopy

For quantification of excitatory synapses, 32 electron micrographs representing 491.9 µm^2 of neuropil regions were taken for each mouse at a magnification of 40,000×. The number of spines (PSD density), proportion of perforated spines, PSD length, and PSD thickness were quantified for each of the three *Ptprd-meB*$^{+/+}$ and three *Ptprd-meB*$^{+/-}$ mice using ImageJ software (NIH). All measurements were performed by an experimenter blind to the genotype.

To quantify the number of VGLUT1-positive axon terminals apposed to PV-positive dendrites (excitatory synaptic density), three blocks were prepared for each mouse. PV-positive dendrites were observed and captured in each block at a magnification of 30,000×. A total of 121 PV-positive dendrites from three Ptprd-meB + /+ mice, and 139 PV-positive dendrites from three Ptprd-meB + /− mice, were captured. For comparison, the total number of VGLUT1-positive axon terminals apposed to PV-positive dendrites were divided by the total perimeter of all observed PV-positive dendrites in each mouse (number of VGLUT1-positive axon terminal / 100 µm, excitatory synaptic density). The perimeter of labeled dendritic shafts was outlined to determine the length of the dendritic membrane using ImageJ software (NIH).

Postsynaptic density fractionation

Postsynaptic density fractionation was conducted to prepare samples for total proteomic analysis. Whole brains, excluding olfactory bulb, cerebellum, and brainstem, were homogenized using a motorized glass/Teflon homogenizer in ice-cold homogenization buffer (0.32 M sucrose, 10 mM HEPES pH 7.4). For the subcellular fractionation of mouse brains, the homogenates were first centrifuged at 900 g for 10 min, yielding pellets (P1). The supernatant from this step was then centrifuged at 12,000 g for 15 min. The resulting pellets were resuspended in the homogenization buffer and centrifuged again at 13,000 g for 15 min to obtain P2, also known as crude synaptosomes. Halt™ protease and phosphatase inhibitor cocktail (Thermo Fisher, 78445) was added to the homogenization buffer before use.

The postsynaptic density (PSD) fractionation was conducted according to the protocol outlined previously[125]. P2 pellets were resuspended and homogenized in double-distilled water (DDW) using a glass/Teflon homogenizer. The pH was quickly adjusted to 7.4 after homogenization, and the samples were subjected to hypoosmotic shock for 30 min. The lysed samples were then ultracentrifuged at 25,000 g for 20 min. The resulting pellet (P3) was resuspended in a 0.32 M HEPES-buffered sucrose solution and carefully layered atop a three-layer (1.2, 1.0, and 0.8 M HEPES-buffered sucrose solution) discontinuous sucrose gradient, followed by ultracentrifugation at 150,000 g for 2 h. The synaptic plasma membrane layer, located between the 1.2 M and 1.0 M sucrose layers, was collected and subjected to ultracentrifugation in a 0.32 M HEPES-buffered sucrose solution at 200,000 g for 30 min. The resulting pellet, referred to as the synaptic plasma membrane (SPM) fraction, was used for total proteomic analysis. The SPM pellet was resuspended in a buffer (50 mM HEPES, 2 mM EDTA) and combined with a detergent solution (0.5% Triton X-100, 50 mM HEPES, 2 mM EDTA) for a 15 min incubation. The mixture was then ultracentrifuged at 32,000 g for 20 min, and the resulting pellet, the postsynaptic density (PSD) fraction, was utilized for total proteomic analysis. All solutions were buffered with HEPES at pH 7.4, except during the hypoosmotic shock with DDW. Halt™ protease and phosphatase inhibitor cocktail was included in every solution. All steps were performed at 4 °C. Ultracentrifugation was conducted using an Optima™ XE-100 (Beckman Coulter) with appropriate swinging-bucket rotors.

Sample preparation for total proteomic analysis

PSD fraction (4 biological replicates each for WT and HT), SPM fraction (4 biological replicates each for WT and HT), and whole lysate (3 biological replicates each for WT and HT) were prepared from the whole brains of WT (*Ptprd-meB*$^{+/+}$) and HT (*Ptprd-meB*$^{+/-}$) mice (postnatal day 63; male), excluding the olfactory bulb, cerebellum, and brainstem. The PSD and SPM pellets were resuspended in 1×sodium dodecyl sulfate (SDS) buffer (5% SDS, 50 mM triethylammonium bicarbonate (TEAB), pH 8.5). Brain tissue was lysed with 1× SDS buffer to obtain

whole lysate samples for total proteomic analysis. Proteins (30 µg for PSD or 300 µg for SPM and whole lysate) were reduced and alkylated with final 10 mM Tris(2-carboxyethyl)phosphine (TCEP) and 20 mM indole 3-acetic acid (IAA). Tryptic digestion was performed using an S-trap mini digestion kit (ProtiFi, Huntington, NY) according to the manufacturer's protocol, employing mass spectrometry-grade Trypsin Gold (Promega, Madison, WI) at a 1:25 trypsin-to-sample ratio. The final eluted samples were dried in a vacuum concentrator and quantified using a Pierce quantitative colorimetric peptide assay kit (Thermo Fisher Scientific, Rockford, IL). Trypsin-digested peptides (10 µg for PSD or 100 µg for SPM and whole lysate) from each sample were labeled using a 10-plex TMT reagent (Thermo Fisher Scientific, Rockford, IL) following the manufacturer's instructions.

Each sample was differentially labeled with TMT tags as follows: 126, 127 N, 127 C, 128 N for WT-PSD; 128 C, 129 N, 129 C, 130 N for HT-PSD; 130 C, 131 for Reference-PSD; 126, 127 C, 128 C, 129 C for WT-SPM; 127 N, 128 N, 129 N, 130 N for HT-SPM; 130 C, 131 for Reference-SPM; 126, 127 C, 128 C for WT-whole lysate; 127 N, 128 N, 129 N for HT-whole lysate; 129 C, 130 N for Reference-whole lysate. For quality control in TMT experiments, reference samples were prepared by pooling equal amounts from each group (PSD, SPM, and whole lysate). A total of 28 samples were prepared using 3 TMT sets, including 2 reference samples per set. Each TMT channel was freshly dissolved in anhydrous acetonitrile (ACN) at a ratio of 0.8:41 (w:v, mg: µL). After incubating for 1 h at room temperature, the reaction was quenched by adding 8 µL of 5% hydroxylamine and incubated for an additional 15 min. Subsequently, samples were combined, dried, and desalted using Pierce peptide desalting spin columns (Thermo Fisher Scientific, Rockford, IL). Total peptides were fractionated into 20 fractions by basic reverse-phase liquid chromatography, and each eluted peptide sample was vacuum dried. For the liquid chromatography-tandem mass spectrometry (LC-MS/MS) analysis, fractionated peptides were diluted by mobile phase A (99.9% water with 0.1% formic acid).

Total proteomic analysis

TMT-labeled samples were combined and fractionated into 20 fractions per TMT set using basic reverse-phase liquid chromatography. A total of 60 fractionated peptides were diluted in mobile phase A (99.9% water with 0.1% formic acid) and analyzed using an Orbitrap Eclipse Tribrid mass spectrometer (Thermo Fisher Scientific) coupled to an UltiMate 3000 RSLCnano system (Thermo Fisher Scientific), equipped with a nanoelectrospray source. This samples are TMT-labeled sample, and therefore, technical replicates were not conducted separately. Samples were loaded onto a PepMap C18 column (Thermo Fisher Scientific) for 140 min at a flow rate of 0.25 µL/min. The mobile phases A and B consisted of 0% and 99.9% acetonitrile, each containing 0.1% formic acid, respectively. During chromatographic separation, the Orbitrap Eclipse was operated in data-dependent mode. The full scan resolution was 120,000 at m/z 400, and the MS2 scans were performed with HCD fragmentation at 37.5% collision energy. The mass range was 400–2000 m/z, and ion transfer tube temperature of 275 °C was used. MS/MS spectra were processed using the Integrated Proteomic Pipeline (IP2, Bruker, version 6.5.5), employing the Uniprot mouse database (Uniprot Release 2022_01). Analysis parameters included a precursor mass tolerance of 20 ppm, a fragment ion mass tolerance of 200 ppm, a minimum of two unique peptide assignments for protein identification, a minimum of six amino acid peptide length, false positive rate of <0.01 at the spectra level, and allowance for up to 1 internal missed cleavage (K and R, tryptic residues). Modification parameters included a static modification of 229.1629 Da at N-terminus, static modifications of 57.02146 Da at C and 229.1629 Da at K residues, and differential modification of 15.9949 Da at M residue. TMT reporter ion mass tolerance was set at 20 ppm. Statistical analysis was conducted using Perseus software (version 1.6.15). Protein expression differences between samples were compared using two-tailed Welch's *t*-test, with the significance threshold set at $P < 0.05$.

Phospho-tyrosine (pTyr) proteomic analysis

Changes in phospho-tyrosine levels of proteins from *Ptprd-meB*$^{+/-}$, *Emx1-Cre;Ptprd-meB*$^{fl/fl}$, and *Vgat-Cre;Ptprd-meB*$^{fl/fl}$ mice (postnatal day 63; male) were determined using the PhosphoScan service provided by Cell Signaling Technology. In brief, whole brains, excluding the olfactory bulb, cerebellum, and brainstem (*Ptprd-meB*$^{+/-}$) or just the cortex and hippocampus (*Emx1-Cre;Ptprd-meB*$^{fl/fl}$ and *Vgat-Cre;Ptprd-meB*$^{fl/fl}$) were extracted and immediately frozen in liquid nitrogen. Samples were shipped to Cell Signaling Technology and homogenized in Urea Lysis Buffer (9 M Urea, 20 mM HEPES pH 8.0, supplemented with a phosphatase inhibitor cocktail). Cells were sonicated and centrifuged to remove insoluble material. Biological replicates were prepared as follows: $n = 3$ mice [WT (*Ptprd-meB*$^{+/+}$), HT (*Ptprd-meB*$^{+/-}$)], 3 [*Ptprd-meB*$^{fl/fl}$, *Emx1-Cre;Ptprd-meB*$^{fl/fl}$], 3 [*Ptprd-meB*$^{fl/fl}$, *Vgat-Cre;Ptprd-meB*$^{fl/fl}$]. Protein concentrations were measured using the Bradford assay, and equal amounts of protein from each sample were used for downstream analysis. Samples were reduced with DTT and alkylated with iodoacetamide. Samples were digested with trypsin (Cell Signaling Technology, #56296), purified using C18 columns (Waters, #WAT051910), and enriched using the PTMScan Phospho-tyrosine pY-1000 Kit (Cell Signaling Technology, #8803). Peptides containing phospho-tyrosine were then eluted for LC-MS/MS analysis.

LC-MS/MS was performed on a Thermo Orbitrap Fusion™ Lumos™ Tribrid™ mass spectrometer with technical duplicate injections for each sample. Peptides were separated on a 50 cm × 100 µm PicoFrit capillary column packed with C18 reversed-phase resin, using a 90-min linear gradient of acetonitrile in 0.125% formic acid at a flow rate of 280 nL/min. Tandem mass spectra were collected in a data-dependent manner using a 3 s cycle time MS/MS method, a dynamic repeat count of one, and a repeat duration of 30 s. Real time recalibration of mass error was performed using lock mass with a singly charged polysiloxane ion $m/z = 371.101237$.

MS spectra were analyzed by Cell Signaling Technology using Comet and the GFY-Core platform (Harvard University). Database searches were performed against the *Mus musculus* Uniprot database (update: 20210303), with a mass accuracy of ± 20 ppm for precursor ions and 0.02 Da for product ions. Cysteine carbamidomethylation was specified as a static modification, while methionine oxidation and phosphorylation of serine, threonine, or tyrosine were specified as variable modifications. Up to 4 missed cleavages and up to 4 variable modifications were allowed per peptide. Results were filtered to a 1% peptide-level FDR with mass accuracy ± 5 ppm on precursor ions and presence of a phosphorylated residue for enriched samples. Site localization confidence was determined using AScore[126]. All quantitative results were generated using Skyline to extract the integrated MS1 peak area of the corresponding peptide assignments[127]. Accuracy of quantitative data was ensured by manual review in Skyline or in the ion chromatogram files. Statistical significance was determined using a two-tailed Student's t-test.

DAVID and SynGO analyses

For DAVID analyses of total proteomics results, proteins that exhibited significant changes (P-value < 0.05 and |fold change (FC)| > 1.2) were identified, and their corresponding gene names were analyzed using DAVID, which offers a comprehensive set of functional annotation tools for understanding the biological significance of gene lists (https://david.ncifcrf.gov/). In the DAVID analysis of phospho-tyrosine proteomics, motifs with significant alterations (P-value < 0.05 and |FC| > 1.5) were identified, and the corresponding gene names were analyzed using DAVID. The results are displayed in bar graphs, illustrating the

biochemical pathway (Kyoto Encyclopedia of Genes and Genomes; KEGG), cellular component (CC), biological process (BP), and molecular function (MF).

For SynGO analyses of total proteomic results, significantly changed proteins (P-value < 0.05 and |FC| > 1.2) were identified, and the corresponding gene names were analyzed using the SynGO, an evidence-based resource for annotation of synaptic proteins (https://www.syngoportal.org). In the SynGO analysis of phospho-tyrosine proteomics, motifs that showed significant changes (P-value < 0.05 and |FC| > 1.5) were identified, and the corresponding gene names were analyzed using SynGO. Enrichment data for each ontology term containing at least 3 genes from the input list were obtained by using a one-sided Fisher exact test and comparison with brain expressed genes as the background set. P-values were adjusted for multiple comparisons through the false discovery rate (FDR) method. The data are presented in sunburst graphs, illustrating the localization (GO, cellular component) and function (GO, biological process). The sunburst graphs display parent and child ontology terms in concentric rings, with more specific terms located towards the outer rings. See the Interactive ontologies section on the home page of https://www.syngoportal.org.

Neuronal culture

Primary cultures of mouse neurons were prepared from embryonic day 18 (E18) male and female WT or *Ptprd-meB*$^{+/-}$ embryos. Dissected hippocampal tissues were maintained in plain neurobasal-A medium (Thermo Fisher Scientific) for 1 day, during which genotyping was performed. Tissues were then dissociated by enzymatic digestion with papain (Worthington Chemical, LS003127). Neurons were plated on a 6-well cell culture plate in plating medium (neurobasal-A medium supplemented with 2% B-27, 10% fetal bovine serum/FBS, 1% GlutaMax, and 1 mM sodium pyruvate; Thermo Fisher Scientific) at a density of 1×10^6 cells per well. After 4 h, the plating medium was replaced with FBS-free culture medium (neurobasal-A medium supplemented with 2% B-27, 1% GlutaMax, and 1 mM sodium pyruvate). Neurons were cultured for 5 days in FBS-free culture medium before being subjected to IL-1β treatment (PeproTech, AF-211-11B). IL-1β was applied at a final concentration of 10 ng/ml for 20 min. For viral infection to confirm *Nlgn3* knockdown efficiency, AAV was applied to WT neurons on days in vitro (DIV) 7, and the cells were harvested on DIV 14.

Statistical analysis

Statistical analyses were conducted with appropriate justifications, and data were evaluated to ensure they met the assumptions of the employed statistical tests. Outliers were identified and excluded using Grubbs' test ($\alpha = 0.05$). For statistical comparison of two groups, the Unpaired t-test, Welch's t-test, or Mann-Whitney test was utilized depending on the data characteristics. Welch's t-test was applied when the two groups exhibited unequal variances. The normality of data distributions was assessed using both the D'Agostino-Pearson omnibus normality test and the Shapiro-Wilk normality test. The Mann-Whitney test was chosen for analyses in any case where either test indicated a p-value of <0.05. For analyses involving two independent variables, two-way ANOVA with the Holm-Sidak multiple-comparisons test was performed. Data are shown as mean ± standard error of mean (SEM). The number of samples (n) is specified in the legend of each figure. Statistical significance is denoted in each figure as follows: $^*P < 0.05$, $^{**}P < 0.01$, and $^{***}P < 0.001$. All statistical tests were performed using Prism 9 (GraphPad), with the exception of DAVID analysis and SynGO analysis. Statistical details are presented in Supplementary Data 1.

Reporting summary

Further information on research design is available in the Nature Portfolio Reporting Summary linked to this article.

Data availability

The mass spectrometry proteomics data generated in this study have been deposited in the ProteomeXchange Consortium via the MassIVE partner repository with the dataset identifier PXD052848 (Total proteomic analysis) [https://massive.ucsd.edu/ProteoSAFe/dataset.jsp?task=43ef149aed3049ae9b781085ededf7ed] and via the PRIDE partner repository with the dataset identifier PXD053554 (Phospho-tyrosine proteomic analysis) [https://www.ebi.ac.uk/pride/archive/projects/PXD053554]. Source data are provided with this paper.

References

1. Südhof, T. C. Towards an understanding of synapse formation. *Neuron* **100**, 276–293 (2018).
2. Südhof, T. C. Synaptic neurexin complexes: a molecular code for the logic of neural circuits. *Cell* **171**, 745–769 (2017).
3. Shen, K. & Scheiffele, P. Genetics and cell biology of building specific synapse connectivity. *Annu. Rev. Neurosci.* **33**, 473–507 (2010).
4. Siddiqui, T. J. & Craig, A. M. Synaptic organizing complexes. *Curr. Opin. Neurobiol.* **21**, 132–143 (2011).
5. de Wit, J. & Ghosh, A. Specification of synaptic connectivity by cell surface interactions. *Nat. Rev. Neurosci.* **17**, 22–35 (2016).
6. Yuzaki, M. Two classes of secreted synaptic organizers in the central nervous system. *Annu Rev. Physiol.* **80**, 243–262 (2018).
7. Kurshan, P. T. & Shen, K. Synaptogenic pathways. *Curr. Opin. Neurobiol.* **57**, 156–162 (2019).
8. Gomez, A. M., Traunmuller, L. & Scheiffele, P. Neurexins: molecular codes for shaping neuronal synapses. *Nat. Rev. Neurosci.* **22**, 137–151 (2021).
9. Um, J. W. & Ko, J. LAR-RPTPs: synaptic adhesion molecules that shape synapse development. *Trends Cell Biol.* **23**, 465–475 (2013).
10. Takahashi, H. & Craig, A. M. Protein tyrosine phosphatases PTPdelta, PTPsigma, and LAR: presynaptic hubs for synapse organization. *Trends Neurosci.* **36**, 522–534 (2013).
11. Yoshida, T. et al. Canonical versus non-canonical transsynaptic signaling of neuroligin 3 tunes development of sociality in mice. *Nat. Commun.* **12**, 1848 (2021).
12. Takahashi, H. et al. Selective control of inhibitory synapse development by Slitrk3-PTPdelta trans-synaptic interaction. *Nat. Neurosci.* **15**, 389–398 (2012).
13. Kwon, S. K., Woo, J., Kim, S. Y., Kim, H. & Kim, E. Trans-synaptic adhesions between netrin-G ligand-3 (NGL-3) and receptor tyrosine phosphatases LAR, protein-tyrosine phosphatase delta (PTPdelta), and PTPsigma via specific domains regulate excitatory synapse formation. *J. Biol. Chem.* **285**, 13966–13978 (2010).
14. Woo, J. et al. Trans-synaptic adhesion between NGL-3 and LAR regulates the formation of excitatory synapses. *Nat. Neurosci.* **12**, 428–437 (2009).
15. Yim, Y. S. et al. Slitrks control excitatory and inhibitory synapse formation with LAR receptor protein tyrosine phosphatases. *Proc. Natl. Acad. Sci. USA* **110**, 4057–4062 (2013).
16. Yoshida, T. et al. Interleukin-1 receptor accessory protein organizes neuronal synaptogenesis as a cell adhesion molecule. *J. Neurosci.* **32**, 2588–2600 (2012).
17. Yoshida, T. et al. IL-1 receptor accessory protein-like 1 associated with mental retardation and autism mediates synapse formation by trans-synaptic interaction with protein tyrosine phosphatase delta. *J. Neurosci.* **31**, 13485–13499 (2011).
18. Li, Y. et al. Splicing-dependent trans-synaptic SALM3-LAR-RPTP interactions regulate excitatory synapse development and locomotion. *Cell Rep.* **12**, 1618–1630 (2015).
19. Choi, Y. et al. SALM5 trans-synaptically interacts with LAR-RPTPs in a splicing-dependent manner to regulate synapse development. *Sci. Rep.* **6**, 26676 (2016).

20. Valnegri, P. et al. The X-linked intellectual disability protein IL1RAPL1 regulates excitatory synapse formation by binding PTPdelta and RhoGAP2. *Hum. Mol. Genet.* **20**, 4797–4809 (2011).
21. Takahashi, H. et al. Postsynaptic TrkC and presynaptic PTPsigma function as a bidirectional excitatory synaptic organizing complex. *Neuron* **69**, 287–303 (2011).
22. Takahashi, H. & Craig, A. Protein tyrosine phosphatases PTPδ, PTPσ, and LAR: presynaptic hubs for synapse organization. *Trends Neurosci.* **36**, 522–34 (2013).
23. Song, Y. S., Lee, H. J., Prosselkov, P., Itohara, S. & Kim, E. Trans-induced cis interaction in the tripartite NGL-1, netrin-G1 and LAR adhesion complex promotes development of excitatory synapses. *J. Cell Sci.* **126**, 4926–4938 (2013).
24. Han, K. A. et al. LAR-RPTPs directly interact with neurexins to coordinate bidirectional assembly of molecular machineries. *J. Neurosci.* **40**, 8438–8462 (2020).
25. Roppongi, R. T. et al. LRRTMs organize synapses through differential engagement of neurexin and PTPσ. *Neuron* **106**, 701 (2020).
26. Won, S. Y. & Kim, H. M. Structural basis for LAR-RPTP-mediated synaptogenesis. *Mol. Cells* **41**, 622–630 (2018).
27. Uhl, G. R. & Martinez, M. J. PTPRD: neurobiology, genetics, and initial pharmacology of a pleiotropic contributor to brain phenotypes. *Ann. N. Y. Acad. Sci.* **1451**, 112–129 (2019).
28. Elia, J. et al. Rare structural variants found in attention-deficit hyperactivity disorder are preferentially associated with neurodevelopmental genes. *Mol. Psychiatry* **15**, 637–646 (2010).
29. Jarick, I. et al. Genome-wide analysis of rare copy number variations reveals PARK2 as a candidate gene for attention-deficit/hyperactivity disorder. *Mol. Psychiatry* **19**, 115–121 (2014).
30. Anney, R. J. et al. Conduct disorder and ADHD: evaluation of conduct problems as a categorical and quantitative trait in the international multicentre ADHD genetics study. *Am. J. Med. Genet B Neuropsychiatr. Genet.* **147B**, 1369–1378 (2008).
31. Distel, M. A. et al. Borderline personality traits and adult attention-deficit hyperactivity disorder symptoms: a genetic analysis of comorbidity. *Am. J. Med. Genet B. Neuropsychiatr. Genet.* **156B**, 817–825 (2011).
32. Choucair, N. et al. Evidence that homozygous PTPRD gene microdeletion causes trigonocephaly, hearing loss, and intellectual disability. *Mol. Cytogenet.* **8**, 39 (2015).
33. Schormair, B. et al. PTPRD (protein tyrosine phosphatase receptor type delta) is associated with restless legs syndrome. *Nat. Genet.* **40**, 946–948 (2008).
34. Yang, Q. et al. Family-based and population-based association studies validate PTPRD as a risk factor for restless legs syndrome. *Mov. Disord.* **26**, 516–519 (2011).
35. Moore, H. T. et al. Periodic leg movements during sleep are associated with polymorphisms in BTBD9, TOX3/BC034767, MEIS1, MAP2K5/SKOR1, and PTPRD. *Sleep* **37**, 1535–1542 (2014).
36. Kim, M. K. et al. Association of restless legs syndrome variants in Korean patients with restless legs syndrome. *Sleep* **36**, 1787–1791 (2013).
37. Jansen, P. R. et al. Genome-wide analysis of insomnia in 1,331,010 individuals identifies new risk loci and functional pathways. *Nat. Genet* **51**, 394–403 (2019).
38. Uhl, G. R. et al. Cocaine reward is reduced by decreased expression of receptor-type protein tyrosine phosphatase D (PTPRD) and by a novel PTPRD antagonist. *Proc. Natl. Acad. Sci. USA* **115**, 11597–11602 (2018).
39. Drgonova, J. et al. Mouse model for protein tyrosine phosphatase D(PTPRD) associations with restless leg syndrome or Willis-Ekbom disease and addiction: reduced expression alters locomotion, sleep behaviors and cocaine-conditioned place preference. *Mol. Med* **21**, 717–725 (2015).
40. Malhotra, D. et al. High frequencies of de novo CNVs in bipolar disorder and schizophrenia. *Neuron* **72**, 951–963 (2011).
41. Mattheisen, M. et al. Genome-wide association study in obsessive-compulsive disorder: results from the OCGAS. *Mol. Psychiatry* **20**, 337–344 (2015).
42. Burton, C. L. et al. Genome-wide association study of pediatric obsessive-compulsive traits: shared genetic risk between traits and disorder. *Transl. Psychiatry* **11**, 91 (2021).
43. Li, W. et al. Genome-wide meta-analysis, functional genomics and integrative analyses implicate new risk genes and therapeutic targets for anxiety disorders. *Nat. Hum. Behav.* **8**, 361–379 (2024).
44. Uetani, N. et al. Impaired learning with enhanced hippocampal long-term potentiation in PTPdelta-deficient mice. *EMBO J.* **19**, 2775–2785 (2000).
45. Park, H. et al. Splice-dependent trans-synaptic PTPdelta-IL1RAPL1 interaction regulates synapse formation and non-REM sleep. *EMBO J.* **39**, e104150 (2020).
46. Han, K. A. et al. Receptor protein tyrosine phosphatase delta is not essential for synapse maintenance or transmission at hippocampal synapses. *Mol. Brain* **13**, 94 (2020).
47. Sclip, A. & Sudhof, T. C. LAR receptor phospho-tyrosine phosphatases regulate NMDA-receptor responses. *Elife* **9**, e53406 (2020).
48. Emperador-Melero, J., de Nola, G. & Kaeser, P. S. Intact synapse structure and function after combined knockout of PTPdelta, PTPsigma, and LAR. *Elife* **10**, e66638 (2021).
49. Han, K. A. et al. Specification of neural circuit architecture shaped by context-dependent patterned LAR-RPTP microexons. *Nat. Commun.* **15**, 1624 (2024).
50. O'Grady, P., Krueger, N. X., Streuli, M. & Saito, H. Genomic organization of the human LAR protein tyrosine phosphatase gene and alternative splicing in the extracellular fibronectin type-III domains. *J. Biol. Chem.* **269**, 25193–25199 (1994).
51. Coles, C. H. et al. Structural basis for extracellular cis and trans RPTPsigma signal competition in synaptogenesis. *Nat. Commun.* **5**, 5209 (2014).
52. Um, J. W. et al. Structural basis for LAR-RPTP/Slitrk complex-mediated synaptic adhesion. *Nat. Commun.* **5**, 5423 (2014).
53. Won, S. Y. et al. LAR-RPTP clustering is modulated by competitive binding between synaptic adhesion partners and heparan sulfate. *Front Mol. Neurosci.* **10**, 327 (2017).
54. Yamagata, A. et al. Structure of Slitrk2-PTPdelta complex reveals mechanisms for splicing-dependent trans-synaptic adhesion. *Sci. Rep.* **5**, 9686 (2015).
55. Goto-Ito, S. et al. Structural basis of trans-synaptic interactions between PTPdelta and SALMs for inducing synapse formation. *Nat. Commun.* **9**, 269 (2018).
56. Karki, S., Paudel, P., Sele, C., Shkumatov, A. V. & Kajander, T. The structure of SALM5 suggests a dimeric assembly for the presynaptic RPTP ligand recognition. *Protein Eng. Des. Sel.* **31**, 147–157 (2018).
57. Lin, Z., Liu, J., Ding, H., Xu, F. & Liu, H. Structural basis of SALM5-induced PTPdelta dimerization for synaptic differentiation. *Nat. Commun.* **9**, 268 (2018).
58. Yamagata, A. et al. Mechanisms of splicing-dependent trans-synaptic adhesion by PTPδ–IL1RAPL1/IL-1RAcP for synaptic differentiation. *Nat. Commun.* **6**, 6926 (2015).
59. Montani, C., Gritti, L., Beretta, S., Verpelli, C. & Sala, C. The synaptic and neuronal functions of the X-linked intellectual disability protein interleukin-1 receptor accessory protein like 1 (IL1RAPL1). *Dev. Neurobiol.* **79**, 85–95 (2019).
60. Nakamura, F. et al. Protein tyrosine phosphatase δ mediates the sema3a-induced cortical basal dendritic arborization through the activation of fyn tyrosine kinase. *J. Neurosci.* **37**, 7125–7139 (2017).

61. Uetani, N., Chagnon, M. J., Kennedy, T. E., Iwakura, Y. & Tremblay, M. L. Mammalian motoneuron axon targeting requires receptor protein tyrosine phosphatases sigma and delta. *J. Neurosci.* **26**, 5872–5880 (2006).
62. Tomita, H. et al. The protein tyrosine phosphatase receptor delta regulates developmental neurogenesis. *Cell Rep.* **30**, 215–228 e215 (2020).
63. Mishra, I. et al. Protein tyrosine phosphatase receptor delta serves as the orexigenic asprosin receptor. *Cell Metab.* **34**, 549–563 e548 (2022).
64. Graf, E. R., Kang, Y., Hauner, A. M. & Craig, A. M. Structure function and splice site analysis of the synaptogenic activity of the neurexin-1β LNS domain. *J. Neurosci.* **26**, 4256–4265 (2006).
65. Boucard, A. A., Chubykin, A. A., Comoletti, D., Taylor, P. & Sudhof, T. C. A splice code for trans-synaptic cell adhesion mediated by binding of neuroligin 1 to alpha- and beta-Neurexins. *Neuron* **48**, 229–236 (2005).
66. Chih, B., Gollan, L. & Scheiffele, P. Alternative splicing controls selective trans-synaptic interactions of the neuroligin-neurexin complex. *Neuron* **51**, 171–178 (2006).
67. Aoto, J., Martinelli, D. C., Malenka, R. C., Tabuchi, K. & Sudhof, T. C. Presynaptic neurexin-3 alternative splicing trans-synaptically controls postsynaptic AMPA receptor trafficking. *Cell* **154**, 75–88 (2013).
68. Dai, J., Aoto, J. & Sudhof, T. C. Alternative splicing of presynaptic neurexins differentially controls postsynaptic NMDA and AMPA receptor responses. *Neuron* **102**, 993–1008.e1005 (2019).
69. Treutlein, B., Gokce, O., Quake, S. R. & Sudhof, T. C. Cartography of neurexin alternative splicing mapped by single-molecule long-read mRNA sequencing. *Proc. Natl. Acad. Sci. USA* **111**, E1291–E1299 (2014).
70. Schreiner, D. et al. Targeted combinatorial alternative splicing generates brain region-specific repertoires of neurexins. *Neuron* **84**, 386–398 (2014).
71. Iijima, T. et al. SAM68 regulates neuronal activity-dependent alternative splicing of neurexin-1. *Cell* **147**, 1601–1614 (2011).
72. Ding, X. et al. Activity-induced histone modifications govern Neurexin-1 mRNA splicing and memory preservation. *Nat. Neurosci.* **20**, 690–699 (2017).
73. Shapiro-Reznik, M., Jilg, A., Lerner, H., Earnest, D. J. & Zisapel, N. Diurnal rhythms in neurexins transcripts and inhibitory/excitatory synapse scaffold proteins in the biological clock. *PLoS ONE* **7**, e37894 (2012).
74. Traunmuller, L., Gomez, A. M., Nguyen, T. M. & Scheiffele, P. Control of neuronal synapse specification by a highly dedicated alternative splicing program. *Science* **352**, 982–986 (2016).
75. Ehrmann, I. et al. The tissue-specific RNA binding protein T-STAR controls regional splicing patterns of neurexin pre-mRNAs in the brain. *PLoS Genet.* **9**, e1003474 (2013).
76. Ko, J., Fuccillo, M. V., Malenka, R. C. & Sudhof, T. C. LRRTM2 functions as a neurexin ligand in promoting excitatory synapse formation. *Neuron* **64**, 791–798 (2009).
77. Siddiqui, T. J., Pancaroglu, R., Kang, Y., Rooyakkers, A. & Craig, A. M. LRRTMs and neuroligins bind neurexins with a differential code to cooperate in glutamate synapse development. *J. Neurosci.* **30**, 7495–7506 (2010).
78. Sugita, S. et al. A stoichiometric complex of neurexins and dystroglycan in brain. *J. Cell Biol.* **154**, 435–445 (2001).
79. Boucard, A. A., Ko, J. & Sudhof, T. C. High affinity neurexin binding to cell adhesion G-protein-coupled receptor CIRL1/latrophilin-1 produces an intercellular adhesion complex. *J. Biol. Chem.* **287**, 9399–9413 (2012).
80. Uemura, T. et al. Trans-synaptic interaction of GluRdelta2 and Neurexin through Cbln1 mediates synapse formation in the cerebellum. *Cell* **141**, 1068–1079 (2010).
81. Li, K., Nakajima, M., Ibanez-Tallon, I. & Heintz, N. A cortical circuit for sexually dimorphic oxytocin-dependent anxiety behaviors. *Cell* **167**, 60–72.e11 (2016).
82. Napolitano, A. et al. Sex differences in autism spectrum disorder: diagnostic, neurobiological, and behavioral features. *Front. Psychiatry* **13**, 889636 (2022).
83. Kissel, L. T. & Werling, D. M. Neural transcriptomic analysis of sex differences in autism spectrum disorder: current insights and future directions. *Biol. Psychiatry* **91**, 53–60 (2020).
84. Ferri, S. L., Abel, T. & Brodkin, E. S. Sex differences in autism spectrum disorder: a review. *Curr. Psychiatry Rep.* **20**, 9 (2018).
85. Bannerman, D. M. et al. Regional dissociations within the hippocampus-memory and anxiety. *Neurosci. Biobehav Rev.* **28**, 273–283 (2004).
86. Kheirbek, M. A. et al. Differential control of learning and anxiety along the dorsoventral axis of the dentate gyrus. *Neuron* **77**, 955–968 (2013).
87. Xiong, G., Metheny, H., Johnson, B. N. & Cohen, A. S. A comparison of different slicing planes in preservation of major hippocampal pathway fibers in the mouse. *Front Neuroanat.* **11**, 107 (2017).
88. Whitebirch, A. C. Acute mouse brain slicing to investigate spontaneous hippocampal network activity. *J. Vis. Exp.* **28**, 162 (2020).
89. Booker, S. A. & Vida, I. Morphological diversity and connectivity of hippocampal interneurons. *Cell Tissue Res.* **373**, 619–641 (2018).
90. Espinoza, C., Guzman, S. J., Zhang, X. & Jonas, P. Parvalbumin(+) interneurons obey unique connectivity rules and establish a powerful lateral-inhibition microcircuit in dentate gyrus. *Nat. Commun.* **9**, 4605 (2018).
91. Yuan, M. et al. Somatostatin-positive interneurons in the dentate gyrus of mice provide local- and long-range septal synaptic inhibition. *Elife* **6**, e21105 (2017).
92. Zipp, F., Nitsch, R., Soriano, E. & Frotscher, M. Entorhinal fibers form synaptic contacts on parvalbumin-immunoreactive neurons in the rat fascia dentata. *Brain Res* **495**, 161–166 (1989).
93. Sambandan, S., Sauer, J. F., Vida, I. & Bartos, M. Associative plasticity at excitatory synapses facilitates recruitment of fast-spiking interneurons in the dentate gyrus. *J. Neurosci.* **30**, 11826–11837 (2010).
94. Scharfman, H. E. The enigmatic mossy cell of the dentate gyrus. *Nat. Rev. Neurosci.* **17**, 562–575 (2016).
95. Houser, C. R., Peng, Z., Wei, X., Huang, C. S. & Mody, I. Mossy cells in the dorsal and ventral dentate gyrus differ in their patterns of axonal projections. *J. Neurosci.* **41**, 991–1004 (2021).
96. Vivar, C. & van Praag, H. Functional circuits of new neurons in the dentate gyrus. *Front. Neural Circuits* **7**, 15 (2013).
97. Woods, N. I. et al. Preferential Targeting of Lateral Entorhinal Inputs onto Newly Integrated Granule Cells. *J. Neurosci.* **38**, 5843–5853 (2018).
98. Tarhan, L. et al. Single cell portal: an interactive home for single-cell genomics data. *bioRxiv* **17**, 2023.07.13.548886 (2023).
99. Habib, N. et al. Div-Seq: Single-nucleus RNA-Seq reveals dynamics of rare adult newborn neurons. *Science* **353**, 925–928 (2016).
100. Chen, K. H., Boettiger, A. N., Moffitt, J. R., Wang, S. & Zhuang, X. RNA imaging. Spatially resolved, highly multiplexed RNA profiling in single cells. *Science* **348**, aaa6090 (2015).
101. Zhang, M. et al. Molecularly defined and spatially resolved cell atlas of the whole mouse brain. *Nature* **624**, 343–354 (2023).
102. Uchigashima, M. et al. Specific Neuroligin3-alphaNeurexin1 signaling regulates GABAergic synaptic function in mouse hippocampus. *Elife* **9**, e59545 (2020).
103. Zhu, Q. et al. Developmental expression and function analysis of protein tyrosine phosphatase receptor type D in oligodendrocyte myelination. *Neuroscience* **308**, 106–114 (2015).
104. Thomas, G. M. & Huganir, R. L. MAPK cascade signalling and synaptic plasticity. *Nat. Rev. Neurosci.* **5**, 173–183 (2004).

105. Asih, P. R. et al. Functions of p38 MAP kinases in the central nervous system. *Front. Mol. Neurosci.* **13**, 570586 (2020).
106. Falcicchia, C., Tozzi, F., Arancio, O., Watterson, D. M. & Origlia, N. Involvement of p38 MAPK in Synaptic Function and Dysfunction. *Int. J. Mol. Sci.* **21**, 5624 (2020).
107. Huang, Y., Smith, D. E., Ibanez-Sandoval, O., Sims, J. E. & Friedman, W. J. Neuron-specific effects of interleukin-1beta are mediated by a novel isoform of the IL-1 receptor accessory protein. *J. Neurosci.* **31**, 18048–18059 (2011).
108. Wang, Y. et al. Adhesion GPCR Latrophilin 3 regulates synaptic function of cone photoreceptors in a trans-synaptic manner. *Proc. Natl. Acad. Sci. USA* **118**, e2106694118 (2021).
109. Wang, S. et al. Alternative splicing of latrophilin-3 controls synapse formation. *Nature* **626**, 128–135 (2024).
110. van den Oord, E. J. et al. A whole methylome CpG-SNP association study of psychosis in blood and brain tissue. *Schizophr. Bull.* **42**, 1018–1026 (2016).
111. Cheng, P. et al. Novel IL1RAP mutation associated with schizophrenia interferes with neuronal growth and related NF-kappaB signal pathways. *Neurosci. Lett.* **775**, 136533 (2022).
112. Cruchaga, C. et al. GWAS of cerebrospinal fluid tau levels identifies risk variants for Alzheimer's disease. *Neuron* **78**, 256–268 (2013).
113. Ramanan, V. K. et al. GWAS of longitudinal amyloid accumulation on 18F-florbetapir PET in Alzheimer's disease implicates microglial activation gene IL1RAP. *Brain* **138**, 3076–3088 (2015).
114. Srinivasan, D., Yen, J. H., Joseph, D. J. & Friedman, W. Cell type-specific interleukin-1beta signaling in the CNS. *J. Neurosci.* **24**, 6482–6488 (2004).
115. Li, Y., Liu, L., Barger, S. W. & Griffin, W. S. Interleukin-1 mediates pathological effects of microglia on tau phosphorylation and on synaptophysin synthesis in cortical neurons through a p38-MAPK pathway. *J. Neurosci.* **23**, 1605–1611 (2003).
116. Beamer, E. & Correa, S. A. L. The p38(MAPK)-MK2 Signaling axis as a critical link between inflammation and synaptic transmission. *Front. Cell Dev. Biol.* **9**, 635636 (2021).
117. Ronkina, N. & Gaestel, M. MAPK-activated protein kinases: servant or partner? *Annu Rev. Biochem.* **91**, 505–540 (2022).
118. Meng, Y. et al. Abnormal spine morphology and enhanced LTP in LIMK-1 knockout mice. *Neuron* **35**, 121–133 (2002).
119. Eales, K. L. et al. The MK2/3 cascade regulates AMPAR trafficking and cognitive flexibility. *Nat. Commun.* **5**, 4701 (2014).
120. Herrera, G., Calfa, G., Schioth, H. B., Lasaga, M. & Scimonelli, T. Memory consolidation impairment induced by Interleukin-1beta is associated with changes in hippocampal structural plasticity. *Behav. Brain Res.* **370**, 111969 (2019).
121. Peitz, M., Pfannkuche, K., Rajewsky, K. & Edenhofer, F. Ability of the hydrophobic FGF and basic TAT peptides to promote cellular uptake of recombinant Cre recombinase: a tool for efficient genetic engineering of mammalian genomes. *Proc. Natl. Acad. Sci. USA* **99**, 4489–4494 (2002).
122. Kim, Y. G., Shin, J. J. & Kim, S. J. Minhee analysis package: an integrated software package for detection and management of spontaneous synaptic events. *Mol. Brain* **14**, 138 (2021).
123. Herzog, E., Takamori, S., Jahn, R., Brose, N. & Wojcik, S. M. Synaptic and vesicular co-localization of the glutamate transporters VGLUT1 and VGLUT2 in the mouse hippocampus. *J. Neurochem.* **99**, 1011–1018 (2006).
124. Steullet, P. et al. Redox dysregulation affects the ventral but not dorsal hippocampus: impairment of parvalbumin neurons, gamma oscillations, and related behaviors. *J. Neurosci.* **30**, 2547–2558 (2010).
125. Au - Bermejo, M. K., Au - Milenkovic, M., Au - Salahpour, A. & Au - Ramsey, A. J. Preparation of synaptic plasma membrane and postsynaptic density proteins using a discontinuous sucrose gradient. *JoVE* **3**, e51896 (2014).
126. Beausoleil, S. A., Villen, J., Gerber, S. A., Rush, J. & Gygi, S. P. A probability-based approach for high-throughput protein phosphorylation analysis and site localization. *Nat. Biotechnol.* **24**, 1285–1292 (2006).
127. MacLean, B. et al. Skyline: an open source document editor for creating and analyzing targeted proteomics experiments. *Bioinformatics* **26**, 966–968 (2010).

Acknowledgements

This work was supported by the National Research Foundation of Korea (NRF-2017R1A5A2015391 to Y.C.B., RS-2024-00400118 to J.B., 202400399013 to J.Y.K), the Korea Institute of Science and Technology Information (KISTI) (K24L2M1C4 to H.P.), and the Institute for Basic Science (IBS-R002-D1 to E.K.).

Author contributions

S.K. performed RT-qPCR and immunoblot experiments; S.K., M.K., Y.Yi, and H.Y.K. performed behavioral experiments; S.K., J.J., and M.K. performed electrophysiological experiments; Y.C. performed EM experiments; S.K. performed PSD fractionation; Y.Yang, H.P., and J.K. performed total proteomic experiments and analyses; S.K. performed phospho-tyrosine proteomic experiments; S.L. performed molecular cloning and neuronal cell culture; J.B., Y.C.B., J.Y.K., and E.K. designed research and wrote the manuscript.

Competing interests

The authors declare no competing interests.

Additional information

Supplementary information The online version contains supplementary material available at https://doi.org/10.1038/s41467-025-59685-3.

Correspondence and requests for materials should be addressed to Eunjoon Kim.

Peer review information *Nature Communications* thanks Shuya Fukai and the other, anonymous, reviewer(s) for their contribution to the peer review of this work. A peer review file is available.